International Journal of Solids and Structures 213 (2021) 25–40

Contents lists available at ScienceDirect

International Journal of Solids and Structures

journal homepage: www.elsevier.com/locate/ijsolstr

# Experimental path-following of equilibria using Newton's method. Part II: Applications and outlook

J. Shen *, R.M.J. Groh, M. Schenk, A. Pirrera

*Bristol Composites Institute (ACCIS), University of Bristol, Queen's Building, University Walk, Bristol BS8 1TR, UK*

ARTICLE INFO

*Article history:*
Received 17 September 2020
Received in revised form 29 October 2020
Accepted 30 November 2020
Available online 11 December 2020

*Keywords:*
Experimental Newton's method
Nonlinear structures
Virtual testing
Stability
Bifurcations

ABSTRACT

In Part I of this paper, a quasi-static experimental path-following method was developed that uses tangent quantities in a feedback controller, based on Newton's method. The ability to compute an experimental tangent stiffness opens the door to more advanced path-following techniques. Here, we extend the experimental path-following method to: (i) pinpointing of critical points (limit and branching points); (ii) branch switching to alternate equilibrium paths; and (iii) tracing of critical points with respect to a secondary parameter. We initially explore these more advanced concepts via the virtual testing environment introduced and validated in Part I. Ultimately, the objective is to demonstrate novel testing procedures and protocols made possible by these advanced experimental path-following methods. In particular, three pertinent examples are discussed: (i) design sensitivity plots for shape-adaptive morphing structures; (ii) validation of nonlinear FE benchmark models; and (iii) non-destructive testing of subcritical (unstable) buckling of thin-walled shells.



## 1. Introduction

Part I of this paper introduced an experimental path-following method using Newton's method for nonlinear structures, based on the use of multiple control points. The additional control points can (i) stabilise otherwise unstable equilibria; (ii) control the shape of the structure; and (iii) provide information about the experimental 'tangential' stiffness matrix of the tested structure. Using this technique, a nonlinear structure can be tested smoothly without inducing snaps at limit points of the main loading parameter; consequently, both stable and unstable equilibria of the nonlinear structure can be path-followed.

Beyond path-following of stable and unstable equilibria, numerical path-following (numerical continuation) techniques allow the stability of structures to be interrogated in a comprehensive manner. For example, extended systems for pinpointing of critical points (Seydel, 1979), branch switching at symmetry-breaking bifurcations (Wagner et al., 1988), and tracing of critical points through parameter space (so-called 'fold lines') (Eriksson, 1994) have been introduced. Similar to the way that the path-following equations for ordinary points (non-critical equilibria) were amended to a displacement-controlled experimental setting in Part I, these extended systems can also be reformulated into feedback control algorithms amenable to experimental path-following. Here, we extend the theoretical aspects of experimental path-following to: (i) pinpointing of critical points on equilibrium paths; (ii) branch switching at bifurcations; and (iii) tracing of critical curves with respect to a secondary loading parameter (fold lines). The feasibility of the developed control algorithms is demonstrated in principle using the virtual testing environment validated in Part I. These extensions bring the features and capabilities of experimental path-following to parity with numerical continuation methods used for design and analysis.

The objective of Part II is to provide an outlook of different testing capabilities that these techniques enable. In particular, by focusing on pertinent example structures we show that the enhanced experimental path-following methodologies outlined herein can be used to: (i) create design sensitivity plots (bifurcation maps) of shape-adaptive morphing structures; (ii) validate nonlinear FE benchmark models; and (iii) create new non-destructive testing and certification paradigms for imperfection-sensitive shells susceptible to subcritical (unstable) buckling. The paper continues with introducing new control algorithms for more advanced experimental path-following. These algorithms are then implemented within the virtual testing environment on three different problems.

## 2. Control Algorithms for Experimental Continuation

In Part I (Shen et al., 2021), we derived the governing equation implemented in the control algorithm for path-following of stable

* Corresponding author.
*E-mail address:* j.shen@bristol.ac.uk (J. Shen).

https://doi.org/10.1016/j.ijsolstr.2020.11.038
0020-7683/

and unstable points, which can be written explicitly in a partitioned form in terms of the incremental displacements at the main actuation $\Delta \boldsymbol{u}_\mathrm{a} = \Delta\lambda \hat{\boldsymbol{u}}_\mathrm{a}$ ($\hat{\boldsymbol{u}}_\mathrm{a}$ being an unchanging reference displacement vector comprising the displacements at all the main actuation points) and probing control points $\Delta \boldsymbol{u}_\mathrm{p}$:

$$\boldsymbol{K}_\mathrm{T}^{\mathrm{pp}} \Delta \boldsymbol{u}_\mathrm{p} + \boldsymbol{K}_\mathrm{T}^{\mathrm{pa}} \hat{\boldsymbol{u}}_\mathrm{a} \Delta\lambda = -\boldsymbol{R}_\mathrm{p}(\boldsymbol{u}_\mathrm{p}, \lambda), \tag{1}$$

where $\boldsymbol{K}_\mathrm{T}^{\mathrm{pp}} = \partial \boldsymbol{R}_\mathrm{p}/\partial \boldsymbol{u}_\mathrm{p}$ and $\boldsymbol{K}_\mathrm{T}^{\mathrm{pa}} = \partial \boldsymbol{R}_\mathrm{p}/\partial \boldsymbol{u}_\mathrm{a}$ are the tangential stiffness matrix components that are approximated using the finite difference method; $\boldsymbol{R}_\mathrm{p}$ is a vector of reaction force readings at the probes.

In the following sections, we discuss how this equation can be extended in an augmented system to pinpoint critical points (Section 2.1), branch switch at symmetry-breaking bifurcations (Section 2.2), and trace fold lines (Section 2.3).

### 2.1. Stability and critical points

During path-following it is expedient to compute the eigenvalues (or a subset of the eigenvalues) of the tangent stiffness matrix $\boldsymbol{K}_\mathrm{T}^{\mathrm{pp}}$. If all eigenvalues are positive, then the equilibrium configuration is (locally) stable. If at least one eigenvalue is negative, then the equilibrium configuration is (locally) unstable. In an experiment, an unstable equilibrium is one where removing the probes causes the structure to instantaneously snap to an alternative equilibrium. If the number of negative eigenvalues changes from one equilibrium state to another, then the experiment must have passed either a limit point or a branching point; for the latter, two or more equilibrium curves intersect.

The location of the singular (critical) point can be pinpointed (to within a numerical tolerance) with one additional Newton step using a bordering equation that describes the singularity of the tangent stiffness matrix. Pinpointing critical points is useful for evaluating snap-through loads more accurately and for ascertaining the existence of bifurcations onto other branches. Furthermore, unfolding of these critical points with respect to additional parameters can provide insights into imperfection and design-parameter sensitivity.

Different bordering equations exist, but all make use of the mathematical definition of the singularity of the tangent stiffness matrix. This is because, using a Taylor series expansion, a small change in the energy potential, $\delta\Pi(\boldsymbol{u}_\mathrm{p}, \lambda)$, due to movements in the probe points, $\delta \boldsymbol{u}_\mathrm{p}$, with the main actuation points held constant (*i.e.* $\lambda = \text{constant}$) is

$$\begin{aligned}\delta\Pi &= \frac{\partial \Pi}{\partial \boldsymbol{u}_\mathrm{p}} \delta \boldsymbol{u}_\mathrm{p} + \frac{1}{2} \delta \boldsymbol{u}_\mathrm{p}^\top \frac{\partial^2 \Pi}{\partial \boldsymbol{u}_\mathrm{p}^2} \delta \boldsymbol{u}_\mathrm{p} + \mathcal{O}(\delta \boldsymbol{u}_\mathrm{p}^3) \\ &= \boldsymbol{R}_\mathrm{p} \delta \boldsymbol{u}_\mathrm{p} + \frac{1}{2} \delta \boldsymbol{u}_\mathrm{p}^\top \boldsymbol{K}_\mathrm{T}^{\mathrm{pp}} \delta \boldsymbol{u}_\mathrm{p} + \mathcal{O}(\delta \boldsymbol{u}_\mathrm{p}^3).\end{aligned} \tag{2}$$

By definition, $\boldsymbol{R}_\mathrm{p} = 0$ for equilibrium, such that the sign of $\delta \boldsymbol{u}_\mathrm{p}^\top \boldsymbol{K}_\mathrm{T}^{\mathrm{pp}} \delta \boldsymbol{u}_\mathrm{p}$ is a sufficient condition for ascertaining the stability of the equilibrium state for small perturbations $\delta \boldsymbol{u}_\mathrm{p}$, *i.e.* local stability. Assuming a symmetric tangent stiffness matrix $\boldsymbol{K}_\mathrm{T}^{\mathrm{pp}}$, a critical point on an equilibrium path with varying parameter $\lambda$ may thus be determined by $\delta \boldsymbol{u}_\mathrm{p}^\top \boldsymbol{K}_\mathrm{T}^{\mathrm{pp}} \delta \boldsymbol{u}_\mathrm{p} = 0$, for some $\delta \boldsymbol{u}_\mathrm{p}$. This coincides with the condition that

$$\det \boldsymbol{K}_\mathrm{T}^{\mathrm{pp}}(\boldsymbol{u}_\mathrm{p}^*, \lambda^*) = 0 \quad \Rightarrow \quad \boldsymbol{K}_\mathrm{T}^{\mathrm{pp}}(\boldsymbol{u}_\mathrm{p}^*, \lambda^*)\boldsymbol{\phi} = \mu\boldsymbol{\phi} = \boldsymbol{0}, \tag{3}$$

where $\mu = 0$ is the eigenvalue that corresponds to the critical eigenvector $\boldsymbol{\phi}$ at the critical point $(\boldsymbol{u}_\mathrm{p}^*, \lambda^*)$.

In order to pinpoint critical points, an extended system is formulated, including the equilibrium Eq. (1) and a singularity condition as the bordering equation, *i.e.* a variant of Eq. (3). The advantage of an extended system is that the singularity condition forces Newton's method to converge to the critical point directly in a single step, provided the starting point is sufficiently close to the singularity. Although bisection techniques have also been developed (Crisfield, 1991; Shi, 1996), these require the calculation of multiple intermediate equilibrium points to hone-in on the singularity, and are thus more time consuming and less amenable to an experimental setting.

One potential bordering equation is the minimally augmented method introduced by Griewank et al. (1984). In the minimally augmented method, the vector equation of Eq. (3) is expressed as its scalar equivalent

$$\mu = \boldsymbol{\phi}^\top \boldsymbol{K}_\mathrm{T}^{\mathrm{pp}} \boldsymbol{\phi} = 0 \tag{4}$$

where $\mu$ is a critical eigenvalue of the symmetric tangent stiffness matrix $\boldsymbol{K}_\mathrm{T}^{\mathrm{pp}}$ and $\boldsymbol{\phi}$ the associated unit-magnitude eigenvector, *i.e.* $\boldsymbol{\phi}^\top \boldsymbol{\phi} = 1$. As is shown later, the solution of the critical-point extended system requires computation of the second derivative of the probe forces $\boldsymbol{R}_\mathrm{p}$. In the present experimental path-following setting, the minimally augmented method introduced by Griewank et al. (1984) is used, because it leads to the least expensive means of computing the second derivative via finite differences. Other common schemes that are used in numerical path-following algorithms—such as the nullvector method, first presented by Seydel (1979)—are also possible but require more finite difference steps; this considerably increases the experimental testing time, as well as the susceptibility to experimental noise and hysteresis.

In the experimental control system, the eigenvalue problem of Eq. (4) is first solved independently, and equilibrium is then sought in a second step while keeping $\mu$ and $\boldsymbol{\phi}$ constant. The eigenvalue problem (the first step) is written as an iterative problem of the form

$$\boldsymbol{K}_\mathrm{T}^{\mathrm{pp}} \boldsymbol{\phi}_{k+1} = \mu_{k+1} \boldsymbol{\phi}_k, \tag{5a}$$

$$\boldsymbol{\phi}_{k+1}^\top \boldsymbol{\phi}_k = 1, \tag{5b}$$

where Eq. (5b) constrains the updated eigenvector to be parallel to the previous one with $||\boldsymbol{\phi}_{k+1}||_2 = ||\boldsymbol{\phi}_k||_2 = 1$. Note, by pre-multiplying Eq. (5a) with $\boldsymbol{\phi}_{k+1}^\top$ and heeding Eq. (5b), we recover the original scalar condition $\mu_{k+1} = \boldsymbol{\phi}_{k+1}^\top \boldsymbol{K}_\mathrm{T}^{\mathrm{pp}} \boldsymbol{\phi}_{k+1}$ of Eq. (4). Thus, Eq. (1) is a valid iterative form of Eq. (4). Eqs. (5a)–(5b) are rearranged into matrix form as follows:

$$\begin{bmatrix} -\boldsymbol{K}_\mathrm{T}^{\mathrm{pp}} & \boldsymbol{\phi}_k \\ \boldsymbol{\phi}_k^\top & 0 \end{bmatrix} \begin{Bmatrix} \boldsymbol{\phi}_{k+1} \\ \mu_{k+1} \end{Bmatrix} = \begin{Bmatrix} \boldsymbol{0} \\ 1 \end{Bmatrix}. \tag{6}$$

In the second step, the equilibrium equations are augmented with the scalar singularity condition of Eq. (4),

$$\boldsymbol{G}(\boldsymbol{u}_\mathrm{p}, \lambda) \equiv \begin{Bmatrix} \boldsymbol{R}_\mathrm{p}(\boldsymbol{u}_\mathrm{p}, \lambda) \\ \mu(\boldsymbol{u}_\mathrm{p}, \lambda) \end{Bmatrix} = \boldsymbol{0}, \tag{7}$$

to find an equilibrium state that satisfies the singularity constraint. Linearising Eq. (7) using the same procedure as for the equilibrium condition $\boldsymbol{R}_\mathrm{p} = \boldsymbol{0}$ in Part I, a critical point $(\boldsymbol{u}_\mathrm{p}^*, \lambda^*)$ is calculated via Newton's method using the iteration matrix

$$\begin{bmatrix} \boldsymbol{K}_\mathrm{T}^{\mathrm{pp}} & \boldsymbol{K}_\mathrm{T}^{\mathrm{pa}} \hat{\boldsymbol{u}}_\mathrm{a} \\ \frac{\partial \mu}{\partial \boldsymbol{u}_\mathrm{p}}^\top & \frac{\partial \mu}{\partial \lambda} \end{bmatrix} \begin{Bmatrix} \Delta \boldsymbol{u}_\mathrm{p} \\ \Delta\lambda \end{Bmatrix} = -\begin{Bmatrix} \boldsymbol{R}_\mathrm{p}(\boldsymbol{u}_\mathrm{p}, \lambda) \\ \mu(\boldsymbol{u}_\mathrm{p}, \lambda) \end{Bmatrix}. \tag{8}$$

The first row of Eq. (8) features the linearised equilibrium problem previously introduced in Part I. The second row features the following derivatives of the singularity equation,

$$\frac{\partial \mu}{\partial \boldsymbol{u}_\mathrm{p}} = \frac{\partial}{\partial \boldsymbol{u}_\mathrm{p}} \left( \boldsymbol{\phi}^\top \boldsymbol{K}_\mathrm{T}^{\mathrm{pp}} \boldsymbol{\phi} \right) = \boldsymbol{\phi}^\top \frac{\partial \boldsymbol{K}_\mathrm{T}^{\mathrm{pp}}}{\partial \boldsymbol{u}_\mathrm{p}} \boldsymbol{\phi} \tag{9a}$$

$$\frac{\partial \mu}{\partial \lambda} = \frac{\partial \mu}{\partial \boldsymbol{u}_\mathrm{a}} \frac{\partial \boldsymbol{u}_\mathrm{a}}{\partial \lambda} = \frac{\partial}{\partial \boldsymbol{u}_\mathrm{a}} \left( \boldsymbol{\phi}^\top \boldsymbol{K}_\mathrm{T}^{\mathrm{pp}} \boldsymbol{\phi} \right) \hat{\boldsymbol{u}}_\mathrm{a} = \boldsymbol{\phi}^\top \left( \frac{\partial \boldsymbol{K}_\mathrm{T}^{\mathrm{pp}}}{\partial \boldsymbol{u}_\mathrm{a}} \hat{\boldsymbol{u}}_\mathrm{a} \right) \boldsymbol{\phi}. \tag{9b}$$

The challenge in experimental path-following is that, contrary to numerical path-following, we do not have direct access to the tangent stiffness. Instead, it is approximated from the probe force measurements by finite differences, and therefore, higher-order finite differences are required to compute the derivatives of the tangent stiffness matrix in Eq. (9).

To compute accurate second-order derivatives of the probe force measurements that preserve (to the extent possible) the quadratic rate of convergence of Newton's method, we make use of directional (Gateaux) derivatives. To accomplish this, recall that the vector $\nabla \boldsymbol{f}(\boldsymbol{x}) \cdot \boldsymbol{v}$ can be formulated as the directional derivative of the vector $\boldsymbol{f}(\boldsymbol{x})$ in the direction of $\boldsymbol{v}$. Hence, using the definition of directional derivatives

$$\nabla \boldsymbol{f}(\boldsymbol{x}) \cdot \boldsymbol{v} = \nabla_{\boldsymbol{v}} \boldsymbol{f}(\boldsymbol{x}) = \frac{\mathrm{d}}{\mathrm{d}\epsilon} \boldsymbol{f}(\boldsymbol{x} + \epsilon \boldsymbol{v}) \Big|_{\epsilon=0} \approx \frac{\boldsymbol{f}(\boldsymbol{x} + \epsilon \boldsymbol{v}) - \boldsymbol{f}(\boldsymbol{x})}{\epsilon}, \tag{10}$$

with $\epsilon$ a small parameter $\ll 1$. Using this definition, the derivatives in Eq. (9) are expressed as

$$\frac{\partial \boldsymbol{K}_{\mathrm{T}}^{\mathrm{pp}}}{\partial \boldsymbol{u}_{\mathrm{p}}} \boldsymbol{\phi} = \nabla_{\boldsymbol{\phi}} \boldsymbol{K}_{\mathrm{T}}^{\mathrm{pp}} = \frac{\mathrm{d}}{\mathrm{d}\epsilon} \boldsymbol{K}_{\mathrm{T}}^{\mathrm{pp}}(\boldsymbol{u}_{\mathrm{p}} + \epsilon \boldsymbol{\phi}, \boldsymbol{u}_{\mathrm{a}}) \Big|_{\epsilon=0} \approx \frac{\boldsymbol{K}_{\mathrm{T}}^{\mathrm{pp}}(\boldsymbol{u}_{\mathrm{p}} + \epsilon \boldsymbol{\phi}, \boldsymbol{u}_{\mathrm{a}}) - \boldsymbol{K}_{\mathrm{T}}^{\mathrm{pp}}(\boldsymbol{u}_{\mathrm{p}}, \boldsymbol{u}_{\mathrm{a}})}{\epsilon} \tag{11a}$$

$$\frac{\partial \boldsymbol{K}_{\mathrm{T}}^{\mathrm{pp}}}{\partial \boldsymbol{u}_{\mathrm{a}}} \hat{\boldsymbol{u}}_{\mathrm{a}} = \nabla_{\hat{\boldsymbol{u}}_{\mathrm{a}}} \boldsymbol{K}_{\mathrm{T}}^{\mathrm{pp}} = \frac{\mathrm{d}}{\mathrm{d}\epsilon} \boldsymbol{K}_{\mathrm{T}}^{\mathrm{pp}}(\boldsymbol{u}_{\mathrm{p}}, \boldsymbol{u}_{\mathrm{a}} + \epsilon \hat{\boldsymbol{u}}_{\mathrm{a}}) \Big|_{\epsilon=0} \approx \frac{\boldsymbol{K}_{\mathrm{T}}^{\mathrm{pp}}(\boldsymbol{u}_{\mathrm{p}}, \boldsymbol{u}_{\mathrm{a}} + \epsilon \hat{\boldsymbol{u}}_{\mathrm{a}}) - \boldsymbol{K}_{\mathrm{T}}^{\mathrm{pp}}(\boldsymbol{u}_{\mathrm{p}}, \boldsymbol{u}_{\mathrm{a}})}{\epsilon}. \tag{11b}$$

By substituting Eq. (11) back into Eq. (9), and using the fact that the tangent stiffness matrix is the gradient of the probe forces with respect to the probe displacements, we can write Eq. (9) as

$$\frac{\partial \mu}{\partial \boldsymbol{u}_{\mathrm{p}}} = \boldsymbol{\phi}^{\top} \nabla_{\boldsymbol{\phi}} \boldsymbol{K}_{\mathrm{T}}^{\mathrm{pp}} = \boldsymbol{\phi}^{\top} \nabla_{\boldsymbol{\phi}} \frac{\partial \boldsymbol{R}_{\mathrm{p}}}{\partial \boldsymbol{u}_{\mathrm{p}}} = \nabla_{\boldsymbol{\phi}\boldsymbol{\phi}} \boldsymbol{R}_{\mathrm{p}} \tag{12a}$$

$$\frac{\partial \mu}{\partial \lambda} = \boldsymbol{\phi}^{\top} \nabla_{\hat{\boldsymbol{u}}_{\mathrm{a}}} \boldsymbol{K}_{\mathrm{T}}^{\mathrm{pp}} \boldsymbol{\phi} = \boldsymbol{\phi}^{\top} \nabla_{\hat{\boldsymbol{u}}_{\mathrm{a}}} \frac{\partial \boldsymbol{R}_{\mathrm{p}}}{\partial \boldsymbol{u}_{\mathrm{p}}} \boldsymbol{\phi} = \boldsymbol{\phi}^{\top} \nabla_{\boldsymbol{\phi}\hat{\boldsymbol{u}}_{\mathrm{a}}} \boldsymbol{R}_{\mathrm{p}}. \tag{12b}$$

These second-order directional derivatives are approximated as follows

$$\frac{\partial \mu}{\partial \boldsymbol{u}_{\mathrm{p}}} \approx \frac{\boldsymbol{R}_{\mathrm{p}}(\boldsymbol{u}_{\mathrm{p}} + \epsilon \boldsymbol{\phi}, \boldsymbol{u}_{\mathrm{a}}) - 2\boldsymbol{R}_{\mathrm{p}}(\boldsymbol{u}_{\mathrm{p}}, \boldsymbol{u}_{\mathrm{a}}) + \boldsymbol{R}_{\mathrm{p}}(\boldsymbol{u}_{\mathrm{p}} - \epsilon \boldsymbol{\phi}, \boldsymbol{u}_{\mathrm{a}})}{\epsilon^2} \tag{13a}$$

$$\frac{\partial \mu}{\partial \lambda} \approx \frac{\boldsymbol{\phi}^{\top}}{\epsilon} \left( \frac{\boldsymbol{R}_{\mathrm{p}}(\boldsymbol{u}_{\mathrm{p}} + \gamma \boldsymbol{\phi}, \boldsymbol{u}_{\mathrm{a}} + \epsilon \hat{\boldsymbol{u}}_{\mathrm{a}}) - \boldsymbol{R}_{\mathrm{p}}(\boldsymbol{u}_{\mathrm{p}}, \boldsymbol{u}_{\mathrm{a}} + \epsilon \hat{\boldsymbol{u}}_{\mathrm{a}})}{\gamma} - \boldsymbol{K}_{\mathrm{T}}^{\mathrm{pp}}(\boldsymbol{u}_{\mathrm{p}}, \boldsymbol{u}_{\mathrm{a}}) \boldsymbol{\phi} \right). \tag{13b}$$

Note that the higher-order derivatives may be sensitive to noise in real experimental scenarios. One potential solution is to adopt Gaussian process regression to create a local model of the response surface on which standard numerical continuation algorithms can then be applied. This method has been demonstrated to be robust to experimental noise and enable tracking of geometric features of the response surface such as folds in nonlinear dynamic experiments (Renson et al., 2019).

The pinpointing process then proceeds as follows. While continuing along an equilibrium path, the eigenvalues of the tangent stiffness matrix are monitored in the control system. When the number of negative eigenvalues between two consecutive equilibrium solutions changes, a critical point must exist between these two converged equilibria, and the pinpointing procedure is started by solving Eq. (8).

Once a critical point has been computed, the nature of the critical point, *i.e.* limit point or bifurcation point, can be determined. Parameterising equilibrium condition $\boldsymbol{R}_{\mathrm{p}} = \boldsymbol{0}$ in terms of an arc-length parameter $s$ and differentiating with respect to this curve parameter gives

$$\dot{\boldsymbol{R}}_{\mathrm{p}}(\boldsymbol{u}_{\mathrm{p}}(s), \lambda(s)) = \frac{\partial \boldsymbol{R}_{\mathrm{p}}}{\partial \boldsymbol{u}_{\mathrm{p}}} \dot{\boldsymbol{u}}_{\mathrm{p}} + \frac{\partial \boldsymbol{R}_{\mathrm{p}}}{\partial \lambda} \dot{\lambda} = \boldsymbol{K}_{\mathrm{T}}^{\mathrm{pp}} \dot{\boldsymbol{u}}_{\mathrm{p}} + \boldsymbol{K}_{\mathrm{T}}^{\mathrm{pa}} \hat{\boldsymbol{u}}_{\mathrm{a}} \dot{\lambda} = \boldsymbol{0}, \tag{14}$$

where a superimposed dot denotes differentiation with respect to $s$. Given the symmetry of $\boldsymbol{K}_{\mathrm{T}}^{\mathrm{pp}}$ and the singularity condition of Eq. (3), pre-multiplication of Eq. (14) by $\boldsymbol{\phi}^{\top}$ at a critical point yields

$$\boldsymbol{\phi}^{\top} \boldsymbol{K}_{\mathrm{T}}^{\mathrm{pp}}(\boldsymbol{u}_{\mathrm{p}}^{*}, \lambda^{*}) \dot{\boldsymbol{u}}_{\mathrm{p}} + \boldsymbol{\phi}^{\top} \boldsymbol{K}_{\mathrm{T}}^{\mathrm{pa}}(\boldsymbol{u}_{\mathrm{p}}^{*}, \lambda^{*}) \hat{\boldsymbol{u}}_{\mathrm{a}} \dot{\lambda} = \left( \boldsymbol{\phi}^{\top} \boldsymbol{K}_{\mathrm{T}}^{\mathrm{pa}}(\boldsymbol{u}_{\mathrm{p}}^{*}, \lambda^{*}) \hat{\boldsymbol{u}}_{\mathrm{a}} \right) \dot{\lambda} = 0. \tag{15}$$

Hence, on an equilibrium path with one changing parameter there can only be two types of critical points—a limit point, *i.e.* a local extremum with $\dot{\lambda} = 0$ and $\boldsymbol{\phi}^{\top} \boldsymbol{K}_{\mathrm{T}}^{\mathrm{pa}} \hat{\boldsymbol{u}}_{\mathrm{a}} \neq 0$, or a bifurcation point, *i.e.* an intersection between two or more distinct equilibrium curves with $\boldsymbol{\phi}^{\top} \boldsymbol{K}_{\mathrm{T}}^{\mathrm{pa}} \hat{\boldsymbol{u}}_{\mathrm{a}} = 0$. If a bifurcation point has been found, we can choose to branch switch onto any of the connected paths. A procedure for doing this is shown in the next section.

### 2.2. Branch switching

If the determined critical point is a branching point, we may place the structure into this critical configuration $\boldsymbol{u}^{*} = (\boldsymbol{u}_{\mathrm{p}}^{*}, \boldsymbol{u}_{\mathrm{a}}^{*})$ and attempt to branch switch. In the case of a simple degeneracy, *i.e.* exactly one zero eigenvalue with two paths intersecting at a branching point, switching from one path to the other is relatively straightforward. For compound instabilities, more advanced methods are required, see *e.g.* Huitfeldt (1991). The simplest method is based on the notion of the nullvector. Namely, if an eigenvector $\boldsymbol{\phi}$ spans the nullspace of the tangent stiffness matrix, *i.e.* $\boldsymbol{K}_{\mathrm{T}}^{\mathrm{pp}} \boldsymbol{\phi} = \boldsymbol{0}$, and if an arbitrary load vector $\boldsymbol{f}$ is in the columnspace of $\boldsymbol{K}_{\mathrm{T}}^{\mathrm{pp}}$, such that $\boldsymbol{K}_{\mathrm{T}}^{\mathrm{pp}} \boldsymbol{u}_{\mathrm{p}} = \boldsymbol{f}$ has a solution $\boldsymbol{u}_{\mathrm{p}} = \bar{\boldsymbol{u}}_{\mathrm{p}}$, then $\boldsymbol{u}_{\mathrm{p}} = \bar{\boldsymbol{u}}_{\mathrm{p}} + \alpha \boldsymbol{\phi}$ is also a solution for any $\alpha \in \mathbb{R}$. Thus, the critical eigenvector at the branching point $\boldsymbol{\phi}$ (corresponding to a zero eigenvalue) computed from the tangent stiffness matrix $\boldsymbol{K}_{\mathrm{T}}^{\mathrm{pp}}$ is used as a perturbation to $\boldsymbol{u}_{\mathrm{p}}^{*}$

$$\boldsymbol{u}_{\mathrm{p}}^{\mathrm{new}} = \boldsymbol{u}_{\mathrm{p}}^{*} + \xi \frac{\boldsymbol{\phi}}{||\boldsymbol{\phi}||_2}. \tag{16}$$

Therefore, the perturbed probing point $\boldsymbol{u}_{\mathrm{p}}^{\mathrm{new}}$ with the main actuation points held constant ($\boldsymbol{u}_{\mathrm{a}}^{\mathrm{new}} = \boldsymbol{u}_{\mathrm{a}}^{*}$) are used as the predictor for the first step onto the new branch. The magnitude of the scaling factor $\xi$ is determined from

$$\xi = \pm \frac{\|\boldsymbol{u}^{*}\|_2}{\rho}, \tag{17}$$

where the sign of $\xi$ controls the direction of path-following along the bifurcated path and $\rho$ is a problem-specific constant in the range of 1–100. Once the predictor has been defined, a converged equilibrium configuration on the new path is determined as outlined in Part I.

### 2.3. Path-following of critical points

Apart from pinpointing critical points for a particular structure, we may also be interested in computing the sensitivity of critical points with respect to another parameter, resulting in a fold line. For example, in the case of a post-buckled Euler column that is snapped from one buckled shape to its inverse, it may be pertinent to assess the sensitivity of the snapping load with respect to the applied compression loading. In this setting, the equilibrium equations $\boldsymbol{R}_{\mathrm{p}}(\boldsymbol{u}_{\mathrm{p}}, \lambda, \zeta) = \boldsymbol{0}$ are written in terms of two active parameters $\lambda$ and $\zeta$—the former being the loading parameter that parametrises the displacement at the main actuation points $\boldsymbol{u}_{\mathrm{a}}$ and the latter parametrising a secondary loading.

A fold line algorithm constrains the equilibrium equations to a curve that unfolds a baseline critical point with respect to the sec-

ondary parameter, *i.e.* a curve describing $(\boldsymbol{u}_\mathrm{p}^*, \lambda^*) = (\boldsymbol{u}_\mathrm{p}^*(\zeta), \lambda^*(\zeta))$. The unfolding of limit and branching points often results in a sequence of critical points of the same nature, limit or branching. For the classic pitchfork bifurcation of the elastica, however, small geometric imperfections can break the pitchfork, thereby transforming the branching point into a limit point. This means that for specific values of the secondary parameter, the unfolding of limit and branching points can lead to sequences of critical points of the other nature. The fold line algorithm presented in this section can handle both types of critical points, such that sequences of limit points only, branching points only, and combinations of limit and branching points can be traced.

Following from the algorithm presented for pinpointing critical points in Section 2.1, the minimally augmented method is used to formulate an extended system to trace along a fold line. The difference to the pinpointing procedure for individual critical points is that $\zeta$ is now introduced as a second parameter. This means that an additional equation needs to be specified to uniquely define the system. This equation takes the form of a path-following constraint. In general, the arc-length constraint may be written as $N(\boldsymbol{u}_\mathrm{p}, \lambda, \zeta) = \boldsymbol{n}_{\boldsymbol{u}_\mathrm{p}}^\top \boldsymbol{u}_\mathrm{p} + n_\lambda \lambda + n_\zeta \zeta - \sigma$, where $\sigma$ is a constant that constrains the arc-length. For example, to retrieve Riks' arc-length equation (Riks, 1979), we define $\boldsymbol{n}_{\boldsymbol{u}_\mathrm{p}}^\top = \Delta \boldsymbol{u}_\mathrm{p}^{(1,k)}$, $n_\lambda = \Delta\lambda^{(1,k)}$ and $n_\zeta = \Delta\zeta^{(1,k)}$, where the $\bullet^{(1,k)}$ quantities are the predictor values of a loading increment $k$. Due to the singularity of each converged equilibrium on a fold line, the predictor values need to be determined using a more involved procedure outlined in Section 2.4.

Introducing the secondary parameter $\zeta$ into the minimally augmented system of Eq. (7), and adding the arc-length constraint, leads to

$$\boldsymbol{G}^N(\boldsymbol{u}_\mathrm{p}, \lambda, \zeta) \equiv \begin{pmatrix} \boldsymbol{R}_\mathrm{p}(\boldsymbol{u}_\mathrm{p}, \lambda, \zeta) \\ \mu(\boldsymbol{u}_\mathrm{p}, \lambda, \zeta) \\ N(\boldsymbol{u}_\mathrm{p}, \lambda, \zeta) \end{pmatrix} = \boldsymbol{0}. \tag{18}$$

Linearisation of Eq. (18) gives

$$\begin{bmatrix} \boldsymbol{K}_\mathrm{T}^{\mathrm{pp}} & \boldsymbol{K}_\mathrm{T}^{\mathrm{pa}}\hat{\boldsymbol{u}}_\mathrm{a} & \frac{\partial \boldsymbol{R}_\mathrm{p}}{\partial \zeta} \\ \frac{\partial \mu}{\partial \boldsymbol{u}_\mathrm{p}}^\top & \frac{\partial \mu}{\partial \lambda} & \frac{\partial \mu}{\partial \zeta} \\ \boldsymbol{n}_{\boldsymbol{u}_\mathrm{p}}^\top & n_\lambda & n_\zeta \end{bmatrix} \begin{Bmatrix} \Delta \boldsymbol{u}_\mathrm{p} \\ \Delta\lambda \\ \Delta\zeta \end{Bmatrix} = -\begin{Bmatrix} \boldsymbol{R}_\mathrm{p}(\boldsymbol{u}_\mathrm{p}, \lambda, \zeta) \\ \mu(\boldsymbol{u}_\mathrm{p}, \lambda, \zeta) \\ N(\boldsymbol{u}_\mathrm{p}, \lambda, \zeta) \end{Bmatrix}, \tag{19}$$

where approximate directional derivatives of $\partial\mu/\partial\boldsymbol{u}_\mathrm{p}$ and $\partial\mu/\partial\lambda$ are computed using Eq. (13). Similarly, using the definition of directional derivatives of Eq. (10), the derivatives with respect to $\zeta$ are

$$\begin{aligned} \frac{\partial \boldsymbol{R}_\mathrm{p}}{\partial \zeta} &= \nabla_\zeta \boldsymbol{R}_\mathrm{p} = \frac{\mathrm{d}}{\mathrm{d}\epsilon} \boldsymbol{R}_\mathrm{p}(\boldsymbol{u}_\mathrm{p}, \lambda, \zeta + \epsilon)\Big|_{\epsilon=0} \\ &\approx \frac{\boldsymbol{R}_\mathrm{p}(\boldsymbol{u}_\mathrm{p}, \lambda, \zeta + \epsilon) - \boldsymbol{R}_\mathrm{p}(\boldsymbol{u}_\mathrm{p}, \lambda, \zeta)}{\epsilon} \end{aligned} \tag{20a}$$

$$\begin{aligned} \frac{\partial \mu}{\partial \zeta} &= \frac{\partial}{\partial \zeta}\left(\boldsymbol{\phi}^\top \boldsymbol{K}_\mathrm{T}^{\mathrm{pp}} \boldsymbol{\phi}\right) = \boldsymbol{\phi}^\top \nabla_\zeta \boldsymbol{K}_\mathrm{T}^{\mathrm{pp}} \boldsymbol{\phi} = \boldsymbol{\phi}^\top \nabla_{\zeta\boldsymbol{\phi}} \boldsymbol{R}_\mathrm{p} \\ &\approx \frac{\boldsymbol{\phi}^\top}{\epsilon}\left(\frac{\boldsymbol{R}_\mathrm{p}(\boldsymbol{u}_\mathrm{p} + \gamma\boldsymbol{\phi}, \lambda, \zeta + \epsilon) - \boldsymbol{R}_\mathrm{p}(\boldsymbol{u}_\mathrm{p}, \lambda, \zeta + \epsilon)}{\gamma} - \boldsymbol{K}_\mathrm{T}^{\mathrm{pp}}(\boldsymbol{u}_\mathrm{p}, \lambda, \zeta)\boldsymbol{\phi}\right). \end{aligned} \tag{20b}$$

To solve the fold line extended system of Eq. (19) efficiently, a partitioning procedure is used such that only the tangent stiffness matrix needs to be factorised. The partitioning procedure is entirely algebraic as shown below. First, the tangent and corrector components of the probe displacements are found via

$$\mathrm{d}\boldsymbol{u}_\mathrm{p} = -\boldsymbol{K}_\mathrm{T}^{\mathrm{pp}^{-1}} \boldsymbol{R}_\mathrm{p}, \quad \delta_\lambda \boldsymbol{u}_\mathrm{p} = -\boldsymbol{K}_\mathrm{T}^{\mathrm{pp}^{-1}} \boldsymbol{K}_\mathrm{T}^{\mathrm{pa}} \hat{\boldsymbol{u}}_\mathrm{a}, \quad \delta_\zeta \boldsymbol{u}_\mathrm{p} = -\boldsymbol{K}_\mathrm{T}^{\mathrm{pp}^{-1}} \frac{\partial \boldsymbol{R}_\mathrm{p}}{\partial \zeta}. \tag{21}$$

Then the parameter increments are found by solving the system

$$\begin{bmatrix} \frac{\partial \mu}{\partial \lambda} + \frac{\partial \mu}{\partial \boldsymbol{u}_\mathrm{p}}^\top \delta_\lambda \boldsymbol{u}_\mathrm{p} & \frac{\partial \mu}{\partial \zeta} + \frac{\partial \mu}{\partial \boldsymbol{u}_\mathrm{p}}^\top \delta_\zeta \boldsymbol{u}_\mathrm{p} \\ \Delta\lambda^{(1,k)} + \Delta \boldsymbol{u}_\mathrm{p}^{(1,k)^\top} \delta_\lambda \boldsymbol{u}_\mathrm{p} & \Delta\zeta^{(1,k)} + \Delta \boldsymbol{u}_\mathrm{p}^{(1,k)^\top} \delta_\zeta \boldsymbol{u}_\mathrm{p} \end{bmatrix} \begin{Bmatrix} \Delta\lambda \\ \Delta\zeta \end{Bmatrix} = -\begin{Bmatrix} \mu + \frac{\partial \mu}{\partial \boldsymbol{u}_\mathrm{p}}^\top \mathrm{d}\boldsymbol{u}_\mathrm{p} \\ \Delta \boldsymbol{u}_\mathrm{p}^{(1,k)^\top} \mathrm{d}\boldsymbol{u}_\mathrm{p} \end{Bmatrix}, \tag{22}$$

which can then be back-substituted to find the probe displacement increment

$$\Delta \boldsymbol{u}_\mathrm{p} = \mathrm{d}\boldsymbol{u}_\mathrm{p} + \Delta\lambda \delta_\lambda \boldsymbol{u}_\mathrm{p} + \Delta\zeta \delta_\zeta \boldsymbol{u}_\mathrm{p}. \tag{23}$$

### 2.4. Tangent vectors to curves

The evaluation of the tangent space is important for predicting the direction of new solutions along an equilibrium path, *i.e.* evaluating the predictor of a loading increment. The tangent space $\mathbf{T}$ of the two-parameter extended system $\boldsymbol{G}(\boldsymbol{u}_\mathrm{p}, \lambda, \zeta) \equiv \boldsymbol{G}(\boldsymbol{y}) = \boldsymbol{0}$, *i.e.* the system without arc-length constraint $N(\boldsymbol{y})$, is given by the nullspace of the differential matrix,

$$\boldsymbol{G}_{\boldsymbol{y}}\mathbf{T} = \boldsymbol{0}. \tag{24}$$

The dimension of $\mathbf{T}$ depends on the number of equations and variables $\boldsymbol{y}$ in the extended system $\boldsymbol{G}(\boldsymbol{y})$. For ordinary (non-critical) equilibrium paths in one parameter, $\lambda$, the tangent space is defined as follows

$$\boldsymbol{G}_{\boldsymbol{y}}\mathbf{T} \equiv \begin{bmatrix} \boldsymbol{K}_\mathrm{T}^{\mathrm{pp}} & \boldsymbol{K}_\mathrm{T}^{\mathrm{pa}}\hat{\boldsymbol{u}}_\mathrm{a} \end{bmatrix} \begin{Bmatrix} \boldsymbol{\tau}_{\boldsymbol{u}_\mathrm{p}} \\ \tau_\lambda \end{Bmatrix} = \boldsymbol{0}. \tag{25}$$

Because there is one more variable than there are equations and the tangent stiffness matrix $\boldsymbol{K}_\mathrm{T}^{\mathrm{pp}}$ is non-singular, a single tangent vector $\boldsymbol{\tau} = [\boldsymbol{\tau}_{\boldsymbol{u}_\mathrm{p}}^\top, \tau_\lambda]^\top$ spans the nullspace $\mathbf{T}$. Solving Eq. (25) gives,

$$\boldsymbol{\tau}_{\boldsymbol{u}_\mathrm{p}} = -\left(\boldsymbol{K}_\mathrm{T}^{\mathrm{pp}^{-1}} \boldsymbol{K}_\mathrm{T}^{\mathrm{pa}} \hat{\boldsymbol{u}}_\mathrm{a}\right)\tau_\lambda = \mathbf{T}_{\boldsymbol{u}_\mathrm{p}} \tau_\lambda, \tag{26}$$

where $\mathbf{T}_{\boldsymbol{u}_\mathrm{p}}$ describes the tangent displacement response of the structure due to an applied load vector $-\boldsymbol{K}_\mathrm{T}^{\mathrm{pa}}\hat{\boldsymbol{u}}_\mathrm{a}$ up to an arbitrary scalar $\tau_\lambda$. At a critical point the nullspace may be of higher dimension due to the singularity of $\boldsymbol{K}_\mathrm{T}^{\mathrm{pp}}$ within $\boldsymbol{G}_{\boldsymbol{y}}$ such that the direction of the curve is not unique. Hence, the special case of fold lines requires careful consideration. For critical fold lines, Eq. (25) reads

$$\boldsymbol{G}_{\boldsymbol{y}}\mathbf{T} \equiv \begin{bmatrix} \boldsymbol{K}_\mathrm{T}^{\mathrm{pp}} & \boldsymbol{K}_\mathrm{T}^{\mathrm{pa}}\hat{\boldsymbol{u}}_\mathrm{a} & \frac{\partial \boldsymbol{R}_\mathrm{p}}{\partial \zeta} \\ \frac{\partial \mu}{\partial \boldsymbol{u}_\mathrm{p}}^\top & \frac{\partial \mu}{\partial \lambda} & \frac{\partial \mu}{\partial \zeta} \end{bmatrix} \begin{Bmatrix} \boldsymbol{\tau}_{\boldsymbol{u}_\mathrm{p}} \\ \tau_\lambda \\ \tau_\zeta \end{Bmatrix} = \boldsymbol{0}, \tag{27}$$

which has no unique solution because the tangent stiffness matrix $\boldsymbol{K}_\mathrm{T}^{\mathrm{pp}}$ is singular at a limit or branching point. The important consideration then becomes which columns $\boldsymbol{K}_\mathrm{T}^{\mathrm{pa}}\hat{\boldsymbol{u}}_\mathrm{a}$ and/or $\partial\boldsymbol{R}_\mathrm{p}/\partial\zeta$ are in the range of $\boldsymbol{K}_\mathrm{T}^{\mathrm{pp}}$. Defining these two columns as $\frac{\partial \boldsymbol{R}_\mathrm{p}}{\partial \boldsymbol{\Lambda}}$ for $\boldsymbol{\Lambda} = (\lambda, \zeta)$, we know that the equation $\boldsymbol{K}_\mathrm{T}^{\mathrm{pp}} \boldsymbol{\tau}_{\boldsymbol{u}_\mathrm{p}} = -\frac{\partial \boldsymbol{R}_\mathrm{p}}{\partial \Lambda_i}$ has a solution $\boldsymbol{\tau}_{\boldsymbol{u}_\mathrm{p}} = \boldsymbol{\tau}'_{\boldsymbol{u}_\mathrm{p}} + \alpha\boldsymbol{\phi}$ for $\alpha \in \mathbb{R}$, if $\frac{\partial \boldsymbol{R}_\mathrm{p}}{\partial \Lambda_i}$ is in the range of $\boldsymbol{K}_\mathrm{T}^{\mathrm{pp}}$. This condition is formally enforced by subtracting from $\frac{\partial \boldsymbol{R}_\mathrm{p}}{\partial \Lambda_i}$ its projection in the direction of the nullvector $\boldsymbol{\phi}$. Hence,

$$\boldsymbol{K}_\mathrm{T}^{\mathrm{pp}}\left(\boldsymbol{\tau}'_{\boldsymbol{u}_{\mathrm{p}_i}} + \alpha\boldsymbol{\phi}\right) = -\left(\boldsymbol{1} - \boldsymbol{\phi}\boldsymbol{\phi}^\top\right)\frac{\partial \boldsymbol{R}_\mathrm{p}}{\partial \Lambda_i}, \tag{28}$$

where $\frac{\partial \boldsymbol{R}'_\mathrm{p}}{\partial \Lambda_i} = \left(\boldsymbol{1} - \boldsymbol{\phi}\boldsymbol{\phi}^\top\right)\frac{\partial \boldsymbol{R}_\mathrm{p}}{\partial \Lambda_i}$ is always in the range of $\boldsymbol{K}_\mathrm{T}^{\mathrm{pp}}$. By choosing the particular solution $\boldsymbol{\tau}'_{\boldsymbol{u}_{\mathrm{p}_i}}$ to be orthogonal to the nullvector we can combine the condition $\boldsymbol{\phi}^\top \boldsymbol{\tau}'_{\boldsymbol{u}_{\mathrm{p}_i}} = 0$ with Eq. (28) to write a system of simultaneous equations

$$\begin{bmatrix} \boldsymbol{K}_{\mathrm{T}}^{\mathrm{pp}} & \boldsymbol{\phi} \\ \boldsymbol{\phi}^{\top} & 0 \end{bmatrix} \begin{Bmatrix} \boldsymbol{\tau}'_{\boldsymbol{u}_{\mathrm{p}_i}} \\ \Pi \end{Bmatrix} = -\begin{Bmatrix} \frac{\partial \boldsymbol{R}_{\mathrm{p}}}{\partial \Lambda_i} \\ 0 \end{Bmatrix}, \tag{29}$$

where we define the projection of $\frac{\partial \boldsymbol{R}_{\mathrm{p}}}{\partial \Lambda_i}$ on the critical eigenvector as $\Pi = -\boldsymbol{\phi}^{\top} \frac{\partial \boldsymbol{R}_{\mathrm{p}}}{\partial \Lambda_i}$ and make use of the fact that $\alpha \boldsymbol{K}_{\mathrm{T}}^{\mathrm{pp}} \boldsymbol{\phi} = \boldsymbol{0}$. The system in Eq. (29) is invertible because the column- and rowspace of $\boldsymbol{K}_{\mathrm{T}}^{\mathrm{pp}}$ are expanded by the nullvector. By solving this system for each control parameter $i = 1, 2$, we can assemble each displacement response $\boldsymbol{\tau}'_{\boldsymbol{u}_{\mathrm{p}_i}}$ into the $i^{th}$ column of a tangent displacement matrix $\mathbf{T}'_{\boldsymbol{u}_{\mathrm{p}}}$ such that the tangent displacement vector is,

$$\boldsymbol{\tau}_{\boldsymbol{u}_{\mathrm{p}}} = \begin{bmatrix} \boldsymbol{\tau}'_{\boldsymbol{u}_{\mathrm{p}_1}} & \boldsymbol{\tau}'_{\boldsymbol{u}_{\mathrm{p}_2}} \end{bmatrix} \begin{Bmatrix} \tau_{\lambda} \\ \tau_{\zeta} \end{Bmatrix} + \alpha \boldsymbol{\phi} = \mathrm{T}'_{\boldsymbol{u}_{\mathrm{p}}} \boldsymbol{\tau}_{\Lambda} + \alpha \boldsymbol{\phi}. \tag{30}$$

Naturally, Eq. (30) needs to satisfy the auxiliary equations (second row of Eq. (27)),

$$\begin{aligned} &\frac{\partial \mu}{\partial \boldsymbol{u}_{\mathrm{p}}}^{\top} \boldsymbol{\tau}_{\boldsymbol{u}_{\mathrm{p}}} + \frac{\partial \mu}{\partial \lambda} \tau_{\lambda} + \frac{\partial \mu}{\partial \zeta} \tau_{\zeta} = \frac{\partial \mu}{\partial \boldsymbol{u}_{\mathrm{p}}}^{\top} \boldsymbol{\tau}_{\boldsymbol{u}_{\mathrm{p}}} + \begin{bmatrix} \frac{\partial \mu}{\partial \lambda} & \frac{\partial \mu}{\partial \zeta} \end{bmatrix} \begin{Bmatrix} \tau_{\lambda} \\ \tau_{\zeta} \end{Bmatrix} \\ &= \frac{\partial \mu}{\partial \boldsymbol{u}_{\mathrm{p}}}^{\top} \left( \mathrm{T}'_{\boldsymbol{u}_{\mathrm{p}}} \boldsymbol{\tau}_{\Lambda} + \alpha \boldsymbol{\phi} \right) + \frac{\partial \mu}{\partial \boldsymbol{\Lambda}} \boldsymbol{\tau}_{\Lambda} \\ &= \left( \frac{\partial \mu}{\partial \boldsymbol{u}_{\mathrm{p}}}^{\top} \mathrm{T}'_{\boldsymbol{u}_{\mathrm{p}}} + \frac{\partial \mu}{\partial \boldsymbol{\Lambda}} \right) \boldsymbol{\tau}_{\Lambda} + \alpha \frac{\partial \mu}{\partial \boldsymbol{u}_{\mathrm{p}}}^{\top} \boldsymbol{\phi} = 0. \end{aligned} \tag{31}$$

Eq. (31) has three unknowns (two parameters and $\alpha$), and therefore two more equations are needed. The first equation is the trivial case of prescribing a unit value for one of the tangent components in $\boldsymbol{\tau}_{\Lambda}$. The second equation is derived from pre-multiplying the first row of Eq. (27) with $\boldsymbol{\phi}^{\top}$ and heeding $\boldsymbol{\phi}^{\top} \boldsymbol{K}_{\mathrm{T}}^{\mathrm{pp}} = \boldsymbol{0}$. Hence,

$$\boldsymbol{\phi}^{\top} \boldsymbol{K}_{\mathrm{T}}^{\mathrm{pp}} \boldsymbol{\tau}_{\boldsymbol{u}_{\mathrm{p}}} + \boldsymbol{\phi}^{\top} \frac{\partial \boldsymbol{R}_{\mathrm{p}}}{\partial \boldsymbol{\Lambda}} \boldsymbol{\tau}_{\Lambda} \equiv \boldsymbol{\phi}^{\top} \frac{\partial \boldsymbol{R}_{\mathrm{p}}}{\partial \boldsymbol{\Lambda}} \boldsymbol{\tau}_{\Lambda} = 0. \tag{32}$$

By introducing a unit value for one of the tangent components in $\boldsymbol{\tau}_{\Lambda}$, Eq. (32) defines a unique proportional relation between the two parameter values.

For most analyses, Eqs. (29), (31) and (32) can be solved for a unique tangent vector. In cases where $\frac{\partial \mu}{\partial \boldsymbol{u}_{\mathrm{p}}}^{\top} \boldsymbol{\phi} = 0$ or $\boldsymbol{\phi}^{\top} \frac{\partial \boldsymbol{R}_{\mathrm{p}}}{\partial \boldsymbol{\Lambda}} = \boldsymbol{0}$ to within a predefined numerical tolerance, the system of equations is singular such that the tangent vector is not uniquely defined. In particular, if $\frac{\partial \mu}{\partial \boldsymbol{u}_{\mathrm{p}}}^{\top} \boldsymbol{\phi} = 0$ then $\alpha$ can not be determined in Eq. (31). Similarly, when $\boldsymbol{\phi}^{\top} \frac{\partial \boldsymbol{R}_{\mathrm{p}}}{\partial \boldsymbol{\Lambda}} = \boldsymbol{0}$ we lose Eq. (32) such that there is one free variable in the system. In both these cases, we set $\alpha = 0$ and solve for $\boldsymbol{\tau}_{\Lambda}$ using Eq. (31) with one parameter component assigned to unity. This situation could, for example, occur at a hilltop-branching point, where a limit and a branching point coincide. Such a case is unlikely to be experienced in a physical experiment.

## 3. Virtual Testing of Experimental Continuation

The virtual testing environment introduced and validated in Part I is here used to demonstrate that the algorithms developed in the previous section can, in principle, be applied in an experimental setting. The simulations highlight novel testing paradigms that are facilitated by these advanced experimental path-following techniques. Further, they are intended as a motivational outlook on the potential impact of these techniques on the experimental mechanics community and the certification of nonlinear structures.

In particular, we focus on three illustrative cases: (i) investigation of the effect of pre-compression on the snap-through load of a curved beam, which has applications in shape-adaptive aerodynamic surfaces; (ii) experimental design for the validation of a classical nonlinear FE benchmark problem with a rich nonlinear response; (iii) introduction of a non-destructive testing framework for axially compressed cylinders, which has applications in the design and testing of launch-vehicle structures.

### 3.1. Effect of pre-compression on a shallow arch

In previous numerical and experimental work, Arena et al. (2017, 2018) showed that a pre-compressed post-buckled beam can be used as a shape-adaptive air inlet. An initially flat beam is buckled into a specific shape that facilitates its function as an air inlet. As air flows at increasing velocity over the post-buckled beam, the aerodynamic pressure increases until it is sufficiently high to snap the beam through into its inverted shape, thereby closing the inlet (see Fig. 1). The beam can be tailored to automatically open again once the air speed falls below a certain threshold. Arena et al. (2018) showed that the air speed at which snap-through and snap-back occurs can be tailored by varying the level of pre-compression in the beam. To demonstrate the relationship between snap-through/snap-back loads and pre-compression, a wind-tunnel experiment had to be repeated in its entirety for varying levels of pre-compression. A complete test run of the nonlinear behaviour for each level of pre-compression proved to be time-consuming. Moreover, a significant amount of additional information was generated that was not required to characterise the behaviour of the structure. Even though the relationship between snap-through/snap-back load and pre-compression can be demonstrated numerically, the strong imperfection sensitivity of nonlin-

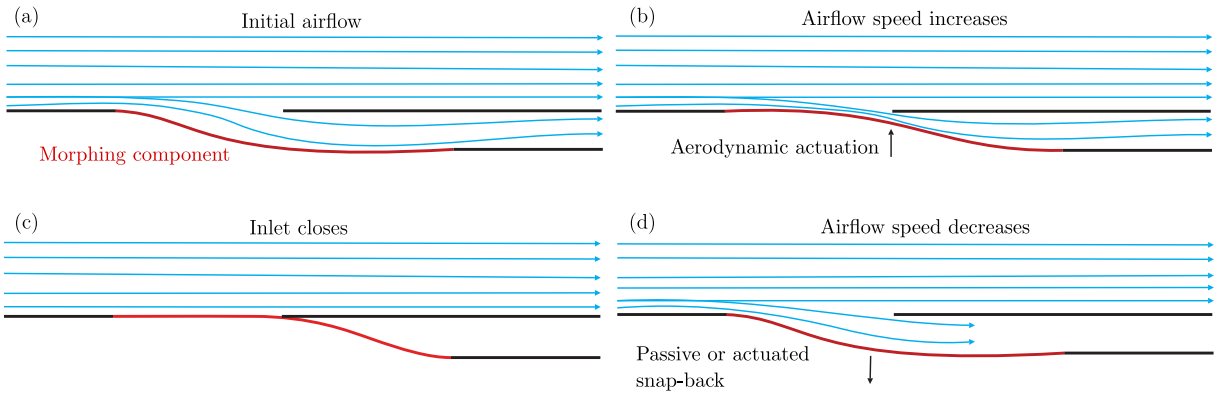


**Fig. 1.** Schematic of a shape-adaptive air inlet. (a) The air inlet with the morphing component (in red) in its open configuration is actuated (b) and closed (c) by the pressure field imposed by a fluid flowing over the curved structure. Depending on the properties of the morphing component, the inlet either remains closed or automatically opens again when the air speed reduces (d). Reproduced from Arena et al. (2017). (For interpretation of the references to colour in this figure legend, the reader is referred to the web version of this article.)

ear systems makes it imperative that key performance parameters, such as snap-through loads, be validated experimentally. This is especially the case if morphing structures, such as the shape-adaptive air inlet, are to be certified for wide-spread industrial use where reliable operation under uncertain conditions is paramount.

As the key parameters in this particular system are the limit points (snap-through & snap-back), the critical point tracking capability (fold line tracing of Section 2.3) would be ideally suited to establish an experimental relationship between snap-through/snap-back loads and pre-compression. In this manner, the key performance parameters of morphing structures, such as the shape-adaptive air inlet, could be validated experimentally in an efficient manner.

To demonstrate the fold line tracking capability, we extend the analysis on the shallow arch presented in Part I by adding a horizontal force to the pinned supports. Geometry and probe layout are presented in Fig. 2a; dimensions and material properties in Table 1. All parameters are as defined in Part I. The horizontal force is equally applied at both supports via horizontal displacement $\Delta_c$, as shown in Fig. 2b. The experimental path-following is implemented in the virtual testing environment outlined in Part I. The arch is modelled in the FE package ABAQUS, but rather than using the embedded quasi-static Riks solver to apply the transverse load at the mid-span and trace the ensuing equilibrium path, the arch deformation is controlled via a sequence of PYTHON scripts that synchronise the movements of the main actuation point (mid-span) and the two linked probe points (one-quarter and three-quarter span). Specifically, nodal displacements are imposed at the arch mid-span to control the main transverse loading, and at the two probe points at the quarter- and three-quarter span to provide shape control and determine the residual forces and tangent stiffness. The control algorithm implements the experimental path-following procedure for ordinary points and critical points, as discussed in Part I and Part II, respectively.

Fig. 3 presents limit points determined using experimental fold line tracing, as well as the full equilibrium paths of the shallow arches with different pre-compression levels obtained using ABAQUS' arc-length solver to obtain an independent benchmark. The results show good correlation. For fold line tracing, a limit point on a single equilibrium curve is determined and pre-compression then varied to balance the control algorithm on the ridge of limit points. The full equilibrium curves obtained by means of ABAQUS' arc-length solver are path-followed in their entirety starting from the unloaded state. The deformed arch configuration at the limit point is shown in Fig. 3b for different levels of pre-compression.

Fig. 4 presents the residual reaction force and critical eigenvalue of the experimental tangent stiffness $\boldsymbol{K}_{\mathrm{T}}^{\mathrm{pp}}$ at the converged limit points for different levels of pre-compression. The convergence condition in the fold line algorithm is set by the residual reaction force at the probes $R_{\mathrm{p}}$. It is observed that the residual reaction force

**Table 1**
Geometric and material properties of the shallow arch. Note that the depth $D$ is into the page. The material is assumed to be linearly elastic, homogeneous and isotropic.

| $L$ (mm) | $h$ (mm) | $t$ (mm) | $D$ (mm) | $E$ (MPa) | $\nu$ |
|---|---|---|---|---|---|
| 205 | 20 | 1.57 | 4.68 | 3200 | 0.38 |

is much smaller than the convergence tolerance limit ($\|R_{\mathrm{p}}\|_2 = 0.01$ N) except for the initial steps. The eigenvalue is also close to zero as required by the definition of a critical point. Note that even more accurate values of the eigenvalue $\mu$ can be obtained by setting an additional tolerance condition on $\mu$ during the corrector steps, as shown by the black squares in Fig. 4. In these cases the final control point corrector displacements are small, and likely to be practically infeasible considering instrument precision and measurement noise.

For verification purposes, the experimental fold line solutions are compared with the solutions from a numerical path-following algorithm (see Groh et al., 2018). As shown in Fig. 5a, the results generally show excellent correlation particularly for the displacement at the actuation point $u_{\mathrm{a,LP}}$. Since $\mathrm{d}F_{\mathrm{a}}/\mathrm{d}u_{\mathrm{a}}$ is infinite at the limit point (see Fig. 3a), a small difference in $u_{\mathrm{a}}$ leads to a disproportionately large difference in $F_{\mathrm{a}}$. This explains the slight discrepancy in the $F_{\mathrm{a,LP}}$ *vs* $\Delta_{\mathrm{c}}$ relationship in the experimental and numerical path-following frameworks in Fig. 5b.

The virtual testing environment reveals that the accuracy of the fold line algorithm is sensitive to the accuracy of the directional derivatives of the reaction force and critical eigenvalue. As these quantities are determined by finite differences, a thorough parameter study is required to determine the best perturbation size to guarantee accurate derivatives, particularly for cases where measurement uncertainty (*e.g.* noise and hysteresis) cannot be neglected.

Finally, we comment on the operational effort of the fold line continuation using the current algorithm. As can be seen in Section 2.3, continuation along the fold line generally demands significant operational efforts in terms of computing derivatives by finite differences. Each finite-difference operation requires a perturbation loading step to compute the small increment away from the currently converged state. Excluding the computation of the tangent stiffness matrix, in the case of the fold line, every predictor and corrector step requires about ten operations, while only one operation is required for path-following of ordinary equilibrium points. In cases where the predictor step falls within the convergence tolerance, the operational burden for fold line continuation is about three times as high as that for ordinary (non-critical) points. However, the critical point pin-pointing process while path-following along an equilibrium path also requires about eight loading operations. Therefore, the fold line continuation is very economic considering it replaces all of the load increments before the critical point.

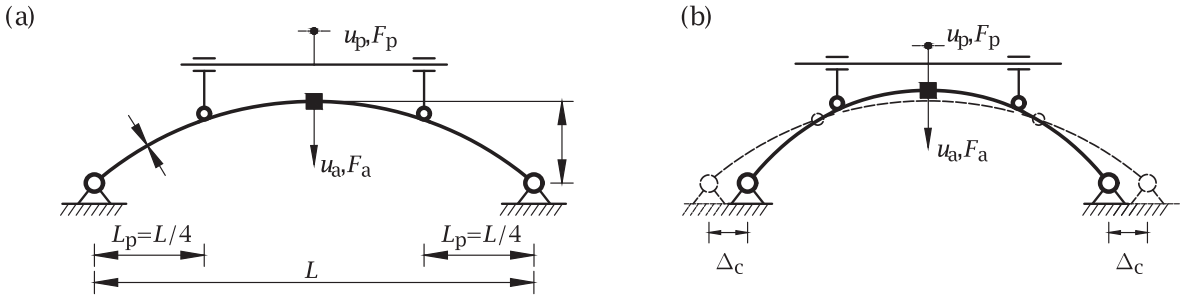


**Fig. 2.** (a) Shallow arch geometry with additional probe points providing shape control while preserving left–right symmetry. (b) Pre-compression applied at the supports via horizontal displacement $\Delta_{\mathrm{c}}$.

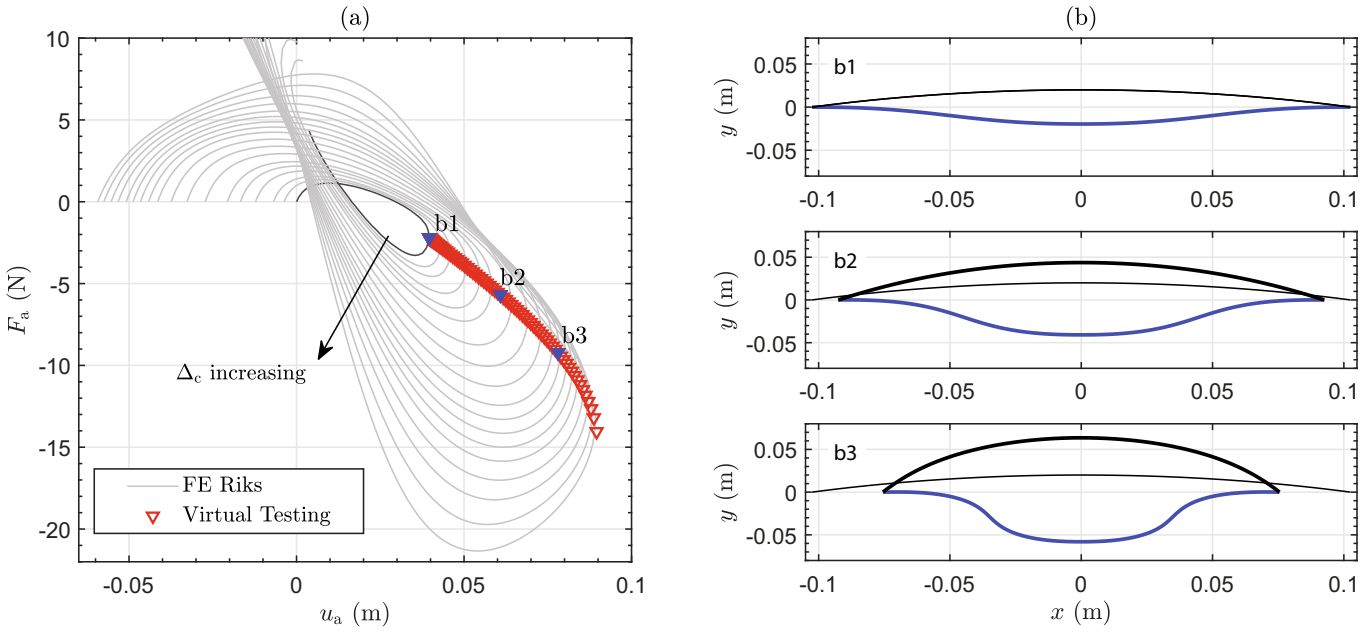


**Fig. 3.** (a) Fold line tracing on a shallow arch with different levels of pre-compression at the supports. $F_a$ and $u_a$ are the reaction force and displacement at the main actuation point, and $\Delta_c$ is the horizontal pre-compression at the supports. The solid lines represent the results obtained from ABAQUS' arc-length solver and triangles represent results from experimental fold line tracing. (b) The deformation shapes of the shallow arch at the limit points (b1–b3 in (a)) for different levels of pre-compression. Thin and thick solid black lines represent the original structural shape and shape with pre-compression only, respectively.

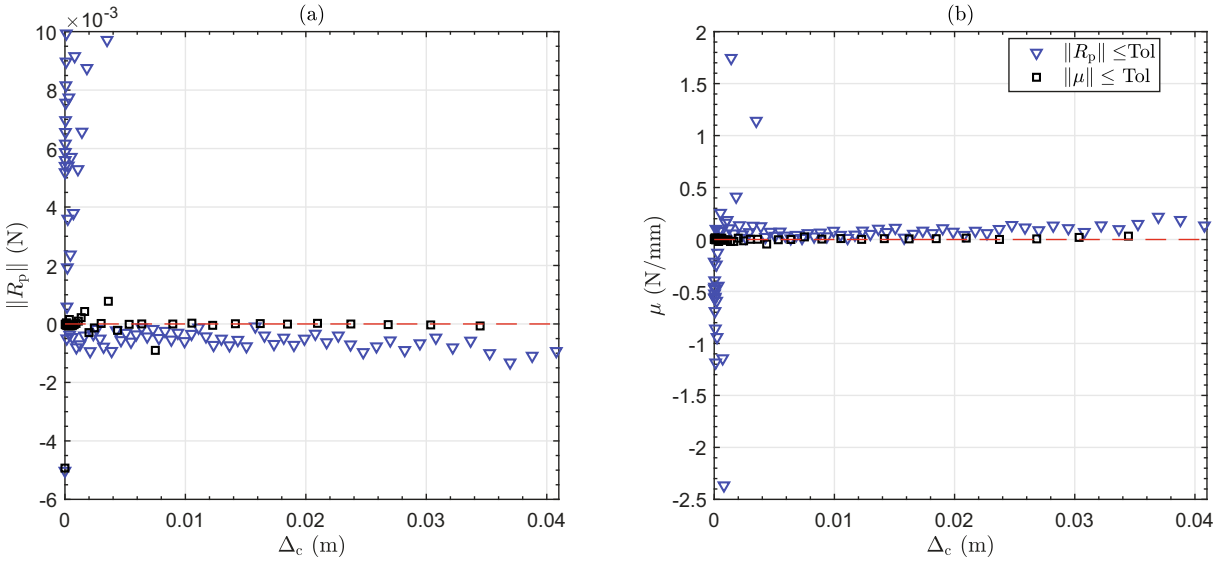


**Fig. 4.** The norm of the residual reaction force $R_p$ and the critical eigenvalue $\mu$ of the experimental tangent stiffness $\boldsymbol{K}_T^{pp}$ at the converged fold line points.

### 3.2. Full equilibrium manifold of a shallow roof

In the computational mechanics community, there are a number of benchmark problems that are used to compare and demonstrate the capabilities of commercial/private finite element codes. One such problem is a hinged, thin, isotropic cylindrical shell point-loaded transversely at its centre, undergoing large displacements and rotations. This particular problem is interesting as it features many of the possible instability phenomena present in shell mechanics; namely, force limit points, displacement limit points, and bifurcations. The benchmark problem was introduced in 1972 and has since been used in numerous articles and books (Crisfield, 1981; Eriksson, 1991; Wardle, 2008; Zhou et al., 2015; Groh et al., 2017). In particular, different finite element formulations have led to slightly different results, raising the question of which formulation is the most accurate throughout the shell's loading history? As discussed by Wardle (2008), for many years only the symmetry-preserving solution was available from FE solvers, whereas experimental specimens would transition onto an asymmetric mode at the first bifurcation, thereby bypassing the force and displacement limit points. Hence, no experimental data exists for verification of the symmetry-preserving benchmark solution featuring limit points. Using the experimental path-following and branch switching capability outlined herein, long-standing FE benchmark problems could be experimentally verified.

In the previous arch example, the symmetrically located probe pairs prevent the possibility of symmetry breaking and branch switching onto bifurcated branches. These constraints are here

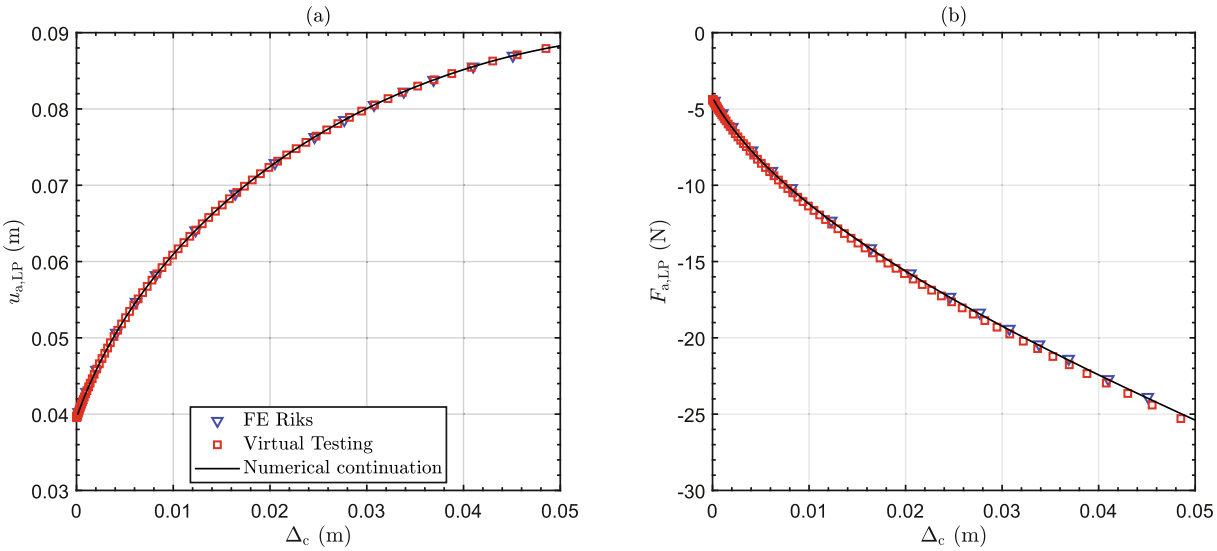


**Fig. 5.** Comparison of the equilibrium states along a fold line as solved from (i) isolating limit points on full equilibrium curves computed in ABAQUS (no probes), (ii) virtual experimental path-following of fold lines (probes) and (iii) numerical path-following of fold lines using a bespoke FE code presented in Groh et al. (2018). Note that for (i) the equilibrium states at the limit point from the FE Riks solver in ABAQUS is approximately determined by adopting the equilibrium state with the largest magnitude of $u_a$.

relaxed such that the full response of the shallow roof can be mapped out. As shown by Zhou et al. (2015) and Groh et al. (2017), there exist two limit points and three pairs of pitchfork bifurcations on the fundamental equilibrium path of the shallow roof. The 'secondary' branches that originate from these three bifurcation points feature additional bifurcations that lead to 'tertiary paths'.

The geometric properties of the shallow roof are summarised in Table 2 and illustrated in Fig. 6a. The longitudinal edges of the roof are pinned and the circumferential edges are free. In the virtual testing environment, the shell roof is modelled using four-node, reduced-integration S4R shell elements within ABAQUS, with a $48 \times 48$ element mesh. Two probe layout schemes are explored, as shown in Fig. 6b–c, respectively. In both cases, four probes are introduced to control the shape of the roof. In the first scheme, two probes with the same $x$-coordinate are coupled, *i.e.* they move up and down simultaneously, to enforce symmetry in the $xz$-plane. For the second scheme, all four probes are independent and the size of the corresponding $\boldsymbol{K}_T^{pp}$ increases to $4 \times 4$. The planar coordinates as well as the probe numbering system are shown in Fig. 6d.

### 3.2.1. Scheme 1: Two independent pairs of probes

To represent an experiment with linked pairs of probes, symmetry boundary conditions are applied to the shell about the $x$-axis (see Fig. 6b). Fig. 7a presents the converged equilibria on the fundamental path and secondary branch from virtual testing, plotted in terms of the transverse displacement $u_a$ *vs* the reaction force $F_a$ at the central actuation point. Blue squares denote stable equilibria (both eigenvalues of the $2 \times 2$ tangent stiffness matrix $\boldsymbol{K}_T^{pp}$ are positive), whereas magenta stars and red triangles represent unstable equilibria with one and two negative eigenvalues in $\boldsymbol{K}_T^{pp}$, respectively. Both limit points on the fundamental path are pin-pointed and unstable equilibria between the limit points are path-followed. Moreover, a pair of bifurcation points is identified and the connecting secondary branch is traced. Fig. 8a–b present the deformed shell in the converged equilibrium state on the fundamental and secondary bifurcation path, respectively. The analysis reveals that a single independent set of probes is sufficient to control the primary path (symmetric mode). This could be achieved by coupling the vertical displacement of all four probes, in which case the size of $\boldsymbol{K}_T^{pp}$ reduces to a scalar.

For verification purposes, nonlinear solutions from the FE Riks solver within ABAQUS are compared with the virtual testing results and good correlation is observed. Currently no critical point pinpointing or branch switching capability is implemented in the Riks solver of ABAQUS. Therefore, in order to trace the secondary branch using ABAQUS, a geometric perturbation of the original geometry using the first eigenmode (left–right asymmetric mode) is introduced.

Fig. 7b presents the eigenvalues and eigenvectors of the experimental tangent stiffness matrix $\boldsymbol{K}_T^{pp}$ along the fundamental equilibrium path. As loading proceeds, the eigenvalue corresponding to a left–right asymmetric mode falls to zero first, corresponding to the first bifurcation point B1. We can branch switch from this critical point B1 with a perturbation profile corresponding to a scaled version of the asymmetric eigenmode, *i.e.* $\boldsymbol{\phi} = [\sqrt{2}/2, -\sqrt{2}/2]$. Beyond B1 on the fundamental path, there is at least one negative eigenvalue until the second bifurcation point B2 is reached, beyond which the equilibrium path remains stable. For the branched secondary path, the number of negative eigenvalues is always zero. Thus, apart from facilitating path-following of ordinary points, the experimental tangent stiffness matrix also provides additional information about the intrinsic stability characteristics of the structure.

The probe layout considered in this section prevents symmetry breaking about the $x$-axis. Therefore, the test setup cannot identify additional bifurcation points along the fundamental path (which do break symmetry). This problem is addressed in the following section by making all four probes independent.

**Table 2**
Geometric and material properties of the example shell roof.

| $R$ (mm) | $L$ (mm) | $t$ (mm) | $\theta$ (rad) | $E$ (N/mm$^2$) | $\nu$ |
|---|---|---|---|---|---|
| 2540 | 508 | 6.35 | 0.1 | 310275 | 0.3 |

### 3.2.2. Scheme 2: Four independent probes

Fig. 9 presents the virtual testing results of the roof with four independent probes. The blue squares denote stable converged equilibria and the other symbols denote unstable converged equi-

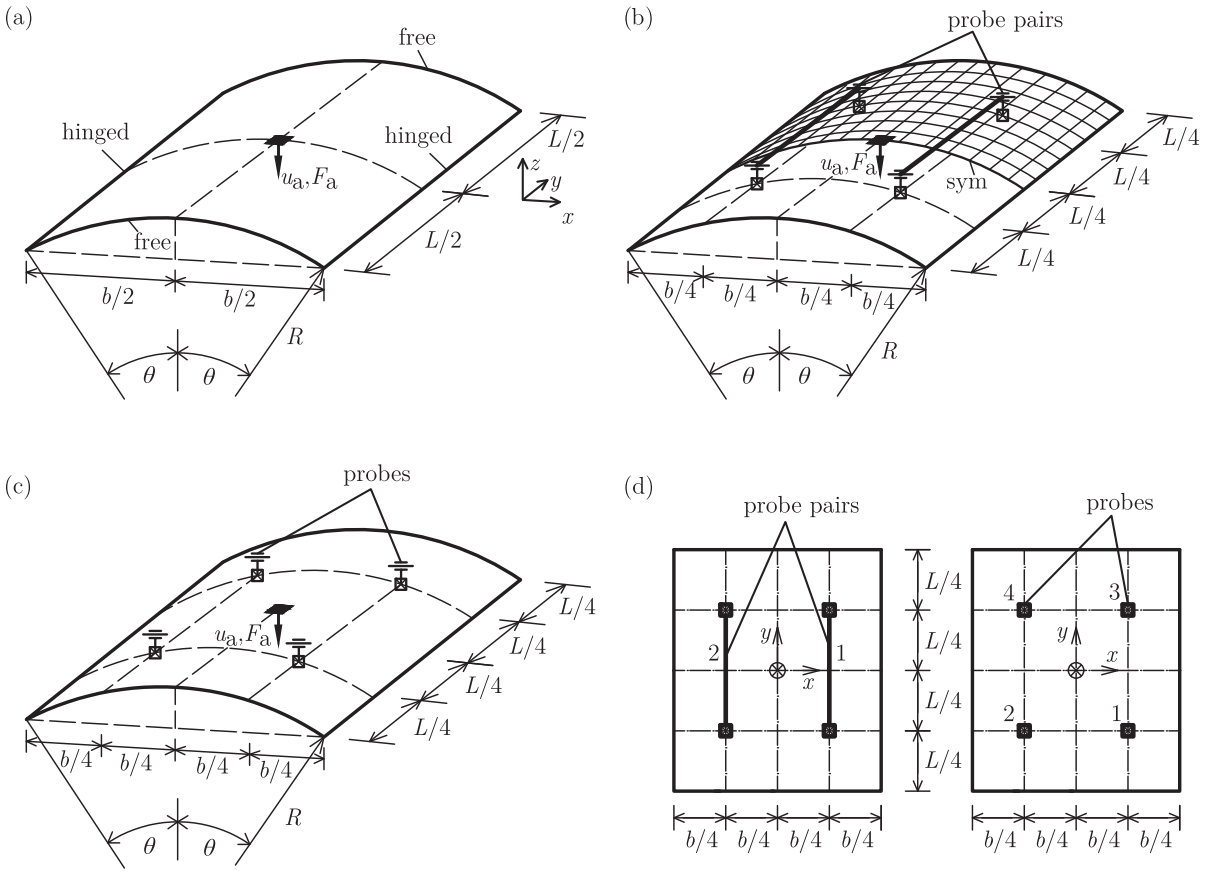


**Fig. 6.** The pinned cylindrical shell roof under a central point load and the layout of probes for shape control. The probes only control the vertical translational displacement and leave all other rotations and displacements free in order to prevent reaction moments and forces that would force the roof into a different equilibrium. (a) Shell roof geometry and boundary conditions; (b) scheme with two independent pairs of probes; (c) scheme with four independent probes; (d) plan view of probe layout and the probe numbering system.

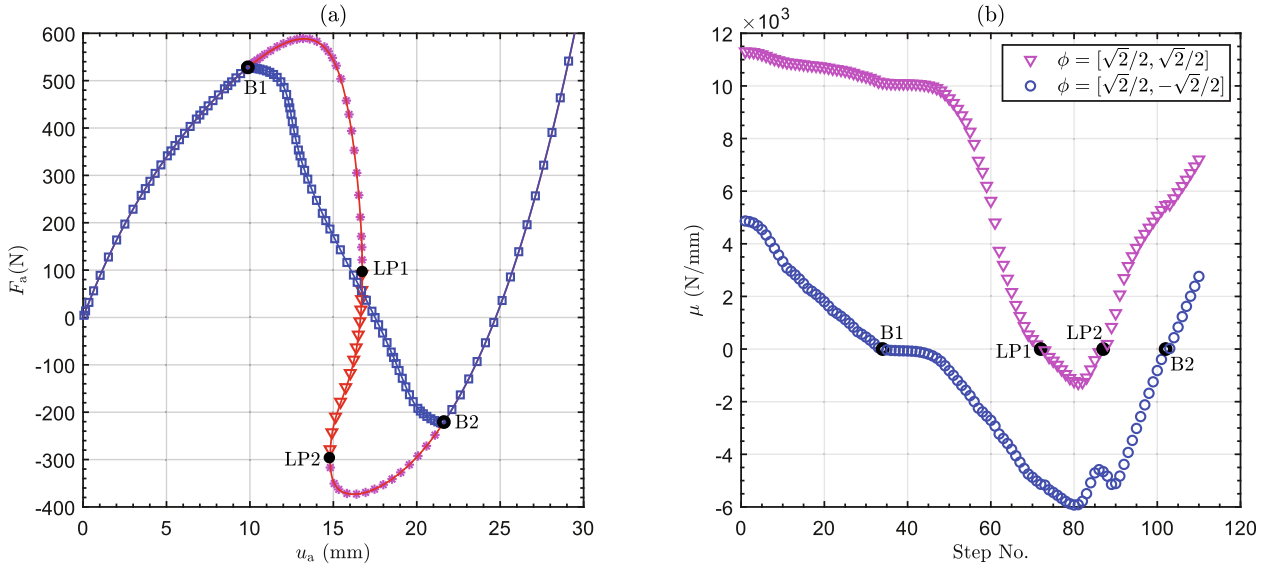


**Fig. 7.** (a) Virtual testing results of the pinned cylindrical roof under a central point load. Squares, stars and triangles represent converged equilibrium states with the zero, one and two negative eigenvalues of the experimental tangent stiffness $\boldsymbol{K}_{\mathrm{T}}^{\mathrm{pp}}$, respectively. Hollow and solid circles represent bifurcation points ('B') and displacement limit points ('LP'), respectively. Solid lines correspond to the solutions from the FE Riks solver in ABAQUS. (b) The eigenvalues and corresponding eigenmodes of the experimental tangent stiffness matrix $\boldsymbol{K}_{\mathrm{T}}^{\mathrm{pp}}$ along the fundamental equilibrium path.

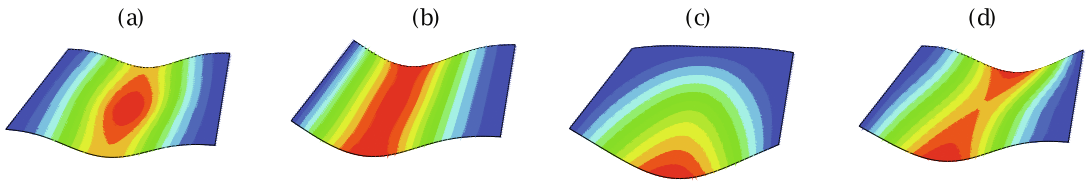


**Fig. 8.** Shell deformation profile along (a) the fundamental path with $u_a = 16.76\,\text{mm}$ and $F_a = 224.35\,\text{N}$; (b) secondary path 2 with $u_a = 16.91\,\text{mm}$ and $F_a = 44.44\,\text{N}$; (c) secondary path 3 with $u_a = 14.86\,\text{mm}$ and $F_a = 172.59\,\text{N}$; and (d) secondary path 4 with $u_a = 15.80\,\text{mm}$ and $F_a = -4.52\,\text{N}$. Contours show vertical deflections, with warmer colours indicating larger values.

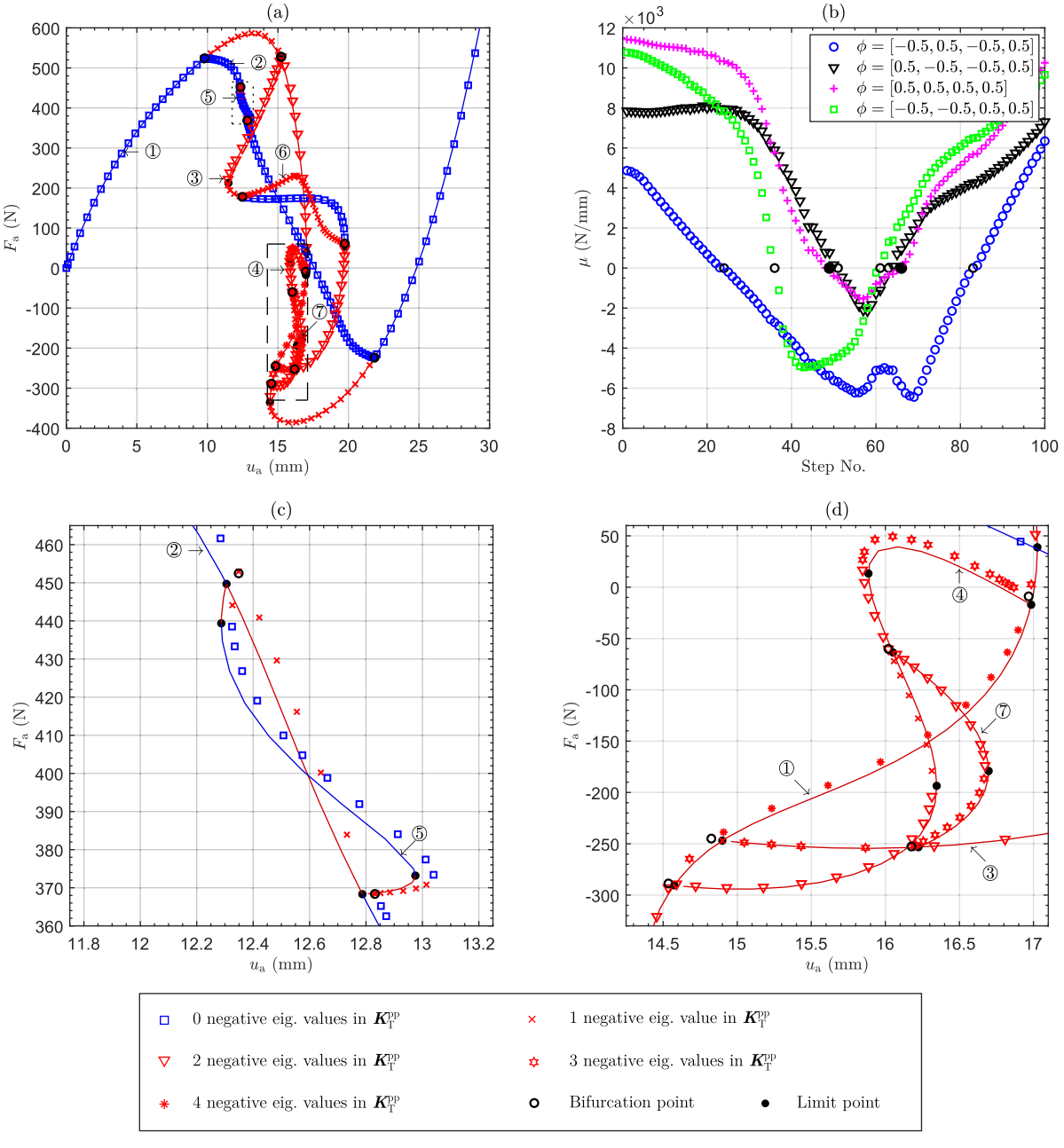


**Fig. 9.** (a,c,d) Virtual testing experimental path-following results of the shallow roof with 4 independent probes. The path numbering system is shown in circles. The numerical continuation solutions (Groh et al., 2018) are superposed as solid curves. Path 1 corresponds to the classical fundamental path; paths 2–4 are secondary branches bifurcating from the fundamental path; and paths 5–7 are tertiary branches emanating from the secondary branches. Squares, crosses, triangles, hexagons and stars represent converged equilibrium states with the number of negative eigenvalues in the experimental tangent stiffness $\boldsymbol{K}_T^{pp}$ equal to zero, one, two, three and four, respectively. Hollow and solid circles represent bifurcation points and limit points, respectively. (b) The eigenvalues and corresponding eigenmodes of the experimental tangent stiffness matrix $\boldsymbol{K}_T^{pp}$ along the fundamental equilibrium path.

libria with at least one negative eigenvalue in $\boldsymbol{K}_{\mathrm{T}}^{\mathrm{pp}}$. In addition to the fundamental path 1 and secondary path 2 identified using two probe pairs, two more sets of bifurcation points and connecting secondary paths (labelled 3 and 4) can be obtained. Deformed configurations of the roof at the converged equilibria on these two additional secondary branches are presented in Fig. 8c–d, respectively. In particular, we access an isolated region of stability on path 3. This isolated region of stability has been identified in two numerical studies (Zhou et al., 2015; Groh et al., 2017) but has not been confirmed experimentally.

Further, we obtain three tertiary paths—labelled 5, 6 and 7 in Fig. 9a, c, d—stemming from secondary paths. Tertiary paths 5 and 6 connect back to the secondary branches from which they originated; tertiary path 7 connects the secondary paths 3 and 4. The eigenvalues and eigenvectors of $\boldsymbol{K}_{\mathrm{T}}^{\mathrm{pp}}$ at each converged equilibrium state along the fundamental path are shown in Fig. 9b. The critical eigenvectors at the bifurcation points on the secondary paths, from which the tertiary paths stem, are listed in Table 3. In particular, the critical eigenvectors on paths 5 and 6 are anti-symmetric about $x$ and $y$ axes respectively, thus breaking the deformation symmetry about the $x$ and $y$ axes on secondary paths 2 and 3.

Results from numerical continuation (Groh et al., 2018) are used for verification of the tertiary paths. Good correlation is observed for all the branches investigated. Discrepancies are a result of the chosen convergence tolerance of the residual reaction force, where $R_{\mathrm{p,tol}} = 0.5$ N. Results with a tighter convergence tolerance are possible but this is unlikely to be feasible in experiments due to the influence of sensor noise.

With four independent probes, the experimental tangent stiffness reflects the complete stability characteristics of the roof as all known bifurcation points are pinpointed, and all secondary and tertiary branches are traced. It should be noted that the curves with eigenvectors $\boldsymbol{\phi} = [-0.5, 0.5, -0.5, 0.5]$ and $\boldsymbol{\phi} = [0.5, 0.5, 0.5, 0.5]$ are essentially the same as for two pairs of probes presented in Fig. 7b, where $\boldsymbol{\phi} = [\sqrt{2}/2, -\sqrt{2}/2]$ and $\boldsymbol{\phi} = [\sqrt{2}/2, \sqrt{2}/2]$ respectively. Since the increase in the number of independent probes makes the experiment less efficient, particularly in the process of determining the experimental tangent stiffness, the experimental efficiency could be improved by coupling probes when only certain equilibrium paths are of interest.

In conclusion, virtual testing of the shallow roof has demonstrated that extended capabilities of experimental path-following, such as the ability to branch switch, could provide the experimental data required to validate classic FE benchmark problems. Furthermore, interesting bifurcation characteristics, such as the isolated regions of stable equilibria observed in numerical studies (Zhou et al., 2015), could be validated experimentally. A demonstrated ability to reach such isolated stable regions also extends the functional capabilities of nonlinear structures.

### 3.3. Non-destructive testing of launch vehicle structures

Cylindrical shells are common structural forms used in the aerospace industry; for example, in primary launch-vehicle structures and for aircraft fuselages. It is well known that cylinders exhibit an extreme sensitivity to initial imperfections (geometric, loading, vibrational perturbations, *etc.*) when loaded in uniaxial compression, such that buckling has a tendency to occur at a fraction of the load predicted by a linearised eigenvalue analysis. The current design of launch vehicle structures is based on conservative, empirically derived safety factors that are used to knock-down the numerical buckling load obtained from an analysis based on an idealised perfect cylinder (Weingarten et al., 1965). Due to the conservative nature of these design codes, significant mass savings are possible if the buckling load of imperfect cylinders can be determined with more certainty, and especially, if this can be done in a non-destructive manner in the laboratory.

Recent computational research on cylinder stability has highlighted the importance of localised buckling modes, so-called 'dimples', on the onset and propagation of buckling (Evkin et al., 2019; Groh and Pirrera, 2019; Kreilos and Schneider, 2017; Wagner et al., 2017). Simultaneously, recent experiments have demonstrated that the rigidity with which a cylinder resists the formation of a single dimple can be interrogated by incorporating a lateral 'poker' in a typical uniaxial compression test (Virot et al., 2017), as shown in Fig. 10. As the cylinder is compressed uniaxially (displacement $u_{\mathrm{a}}$) a poker perturbs the cylinder laterally (displacement $u_{\mathrm{p}}$). By

**Table 3**
Critical eigenvectors at the bifurcation points connecting secondary and tertiary paths. Subscripts 'start' and 'end' represent the loading sequence.

| Path No. | $\boldsymbol{\phi}_{\mathrm{start}}$ | | | | $\boldsymbol{\phi}_{\mathrm{end}}$ | | | |
|---|---|---|---|---|---|---|---|---|
| | 1 | 2 | 3 | 4 | 1 | 2 | 3 | 4 |
| 5 | 0.6917 | 0.1468 | −0.6917 | −0.1468 | −0.6686 | −0.2282 | 0.6686 | 0.2282 |
| 6 | −0.1912 | 0.1912 | -0.6807 | 0.6807 | 0.5760 | -0.5760 | 0.4101 | −0.4101 |
| 7 | −0.6894 | 0.1571 | −0.1571 | 0.6894 | 0.2724 | −0.2724 | −0.6520 | 0.6520 |

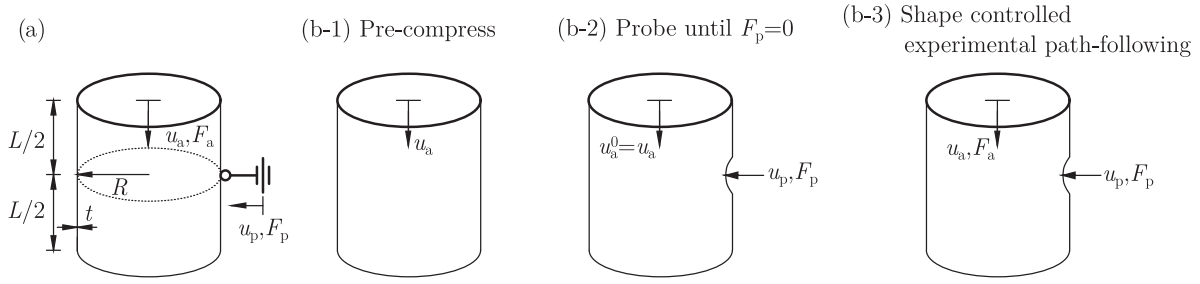


**Fig. 10.** (a) An axially compressed isotropic cylinder of radius $R$, length $L$, thickness $t$ and Young's modulus $E$, loaded by a controlled axial displacement $u_{\mathrm{a}}$ and a lateral poking displacement $u_{\mathrm{p}}$ at the cylinder mid-length that creates a dimple and induces a reaction force $F_{\mathrm{p}}$. (b1–b3) Procedure for non-destructive testing of the cylinder. (b-1) Compress the cylinder axially until the level of compression is 50–70% of the classical buckling load. (b-2) Move the poker located at the mid-height of the cylinder inward until the reaction force at the poker becomes zero (falls below a tolerance). (b-3) Use the final state in (b-2) as the starting point for tracing the unstable single-dimple solution using the experimental continuation technique.

measuring the reaction force $F_p$ on the poker, the unstable equilibrium corresponding to a single dimple can be determined when the reaction force on the poker falls to zero, $F_p = 0$. By repeating this sequence for different levels of axial compression, a stability landscape can be determined, as shown in Fig. 11, which highlights a number of key features that govern the buckling behaviour of axially compressed shells.

The single dimple first exists as a possible equilibrium state in the post-buckling regime beyond a specific threshold of axial compression. For levels of axial compression much smaller than this threshold, the reaction force *vs* displacement of the poker describes a curve of purely positive stiffness (see path 1 in Fig. 11a). Slightly below the single-dimple threshold, the poker reaction force *vs* poker displacement relationship is sigmoidal with two force limit points, a maximum and a minimum, but the curve does not cross the zero reaction force axis (see paths 2 and 3 in Fig. 11a). For levels of compression above the single-dimple threshold, the poker reaction force *vs* poker displacement curve is still sigmoidal but now passes through the zero reaction force axis (see path 4 in Fig. 11a). The locus of points that connects the maximum limit points is a fold line (see Fig. 11b)—the so-called 'ridge' (Virot et al., 2017)—that intuitively describes the rigidity of the cylinder to resist lateral perturbations. Indeed, when the ridge intersects the zero poker reaction force axis, the cylinder provides no resistance to lateral disturbances; by definition, the buckling point (BP in Fig. 11b) has been reached. Thus, the point where the ridge intersects the poker reaction force axis can be used as a prediction of the buckling load of imperfect cylinders.

Within the current displacement-based experimental path-following framework, it is not possible to trace this ridge, a fold line of force limit points. However, by synchronising the axial displacement $u_a$ and poker displacement $u_p$, we are able to trace the single-dimple equilibrium curve with the condition that the residual reaction force at the poker is zero. As shown in Fig. 11b, for increasing $u_a$ the single-dimple equilibrium value of $u_p$ decreases, and the point where $u_p = 0$ can thus be used as a prediction of the critical buckling load $u_{a,cr}$. To prevent buckling of the cylinder during the experiment, and thus to guarantee non-destructive testing, the experimental path-following procedure is terminated once the poker displacement $u_p$ falls below a specified threshold. In order to predict the buckling load, the converged equilibria obtained are then extrapolated to derive the level of axial compression where the poker displacement falls to zero.

The geometric and material properties of the cylindrical shell investigated are the same as those adopted by Virot et al. (2017), as summarised in Table 4. In the virtual testing experiment the cylinder is modelled using four-node shell elements (120 circumferential × 72 axial elements), and has pinned boundary supports. Fig. 10 presents the experimental procedure for the virtual testing. The cylinder is initially compressed to 50%–70% of the classical buckling load, $P_{cr} = 2\pi Et^2/\sqrt{3(1-\nu^2)}$, and to a level above the single dimple threshold. A poker is attached at the mid-length of the cylinder, and is moved radially inwards while keeping the level of axial compression fixed. As presented in Fig. 11a, the reaction force initially increases and then decreases with poker displacement. The poking process ends when the reaction force at the poker $F_p$ becomes zero. Compared with the setup in Virot et al. (2017), the poker is bi-directional and can both push and pull. This means that the otherwise unstable single-dimple solution with $F_p = 0$ can be stabilised. Once this equilibrium state is obtained, the experimental path-following technique is adopted to trace the unstable single-dimple solution with varying axial compression and dimple depth. Here, the poker assumes the function of a probe required for shape control.

Fig. 12 presents the virtual testing results for a perfect cylindrical shell (no geometric imperfections). The cylinder is loaded to 51% of the classical buckling load; then, the poker is moved inwards with constant axial compression until the poker reaction force is zero (falls below a tolerance), indicated by the red triangle in Fig. 12a. Note that this equilibrium state is unstable and removing the poker would lead to buckling of the shell. Next, the experimental path-following is initiated in the direction of increasing $u_a$. As shown in Fig. 12b, the poker displacement $u_p$ decreases with

**Table 4**
Geometric and material properties of the cylindrical shell.

| $R$ (mm) | $L$ (mm) | $t$ (mm) | $E$ (N/mm$^2$) | $\nu$ |
|---|---|---|---|---|
| 28.6 | 107 | 0.104 | 210000 | 0.3 |

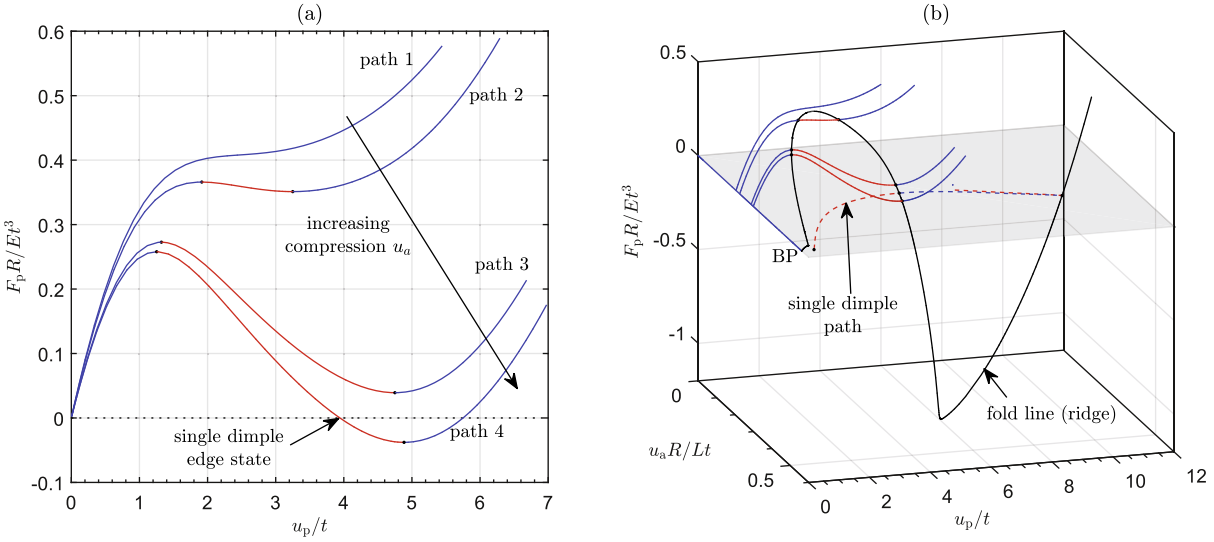


**Fig. 11.** Stability landscape of the axially compressed cylinder with a controlled axial displacement $u_a$ and a lateral poking displacement $u_p$ at the cylinder mid-length, as presented in Fig. 10a. (a) Poking force $F_p$ *vs* dimple displacement $u_p$ for different levels of compression $u_a$. (b) The three-dimensional stability landscape as a function of $u_a, F_p$ and $u_p$. Note that black dots in (a) represent the force limit point, which separates stable (blue lines) and unstable (red lines) equilibria. (For interpretation of the references to colour in this figure legend, the reader is referred to the web version of this article.)

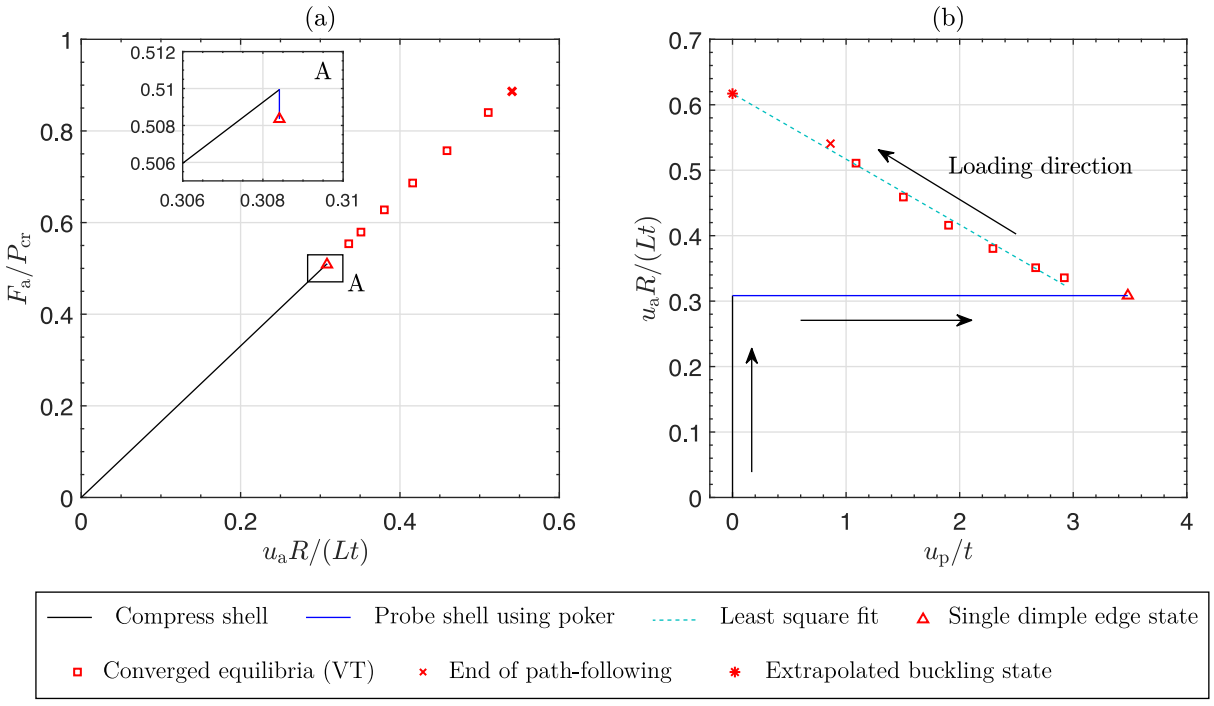


**Fig. 12.** Virtual non-destructive testing results of the perfect cylindrical shell (no geometric imperfections). (a) The load–end-shortening relationship at the actuation point in the pre-buckling regime, poking regime and the single-dimple post-buckling regime. Triangles and crosses represent the start and end of the experimental path-following process. (b) The relationship of the actuation point and poker displacement during testing. Arrows represent the loading direction. Symbol star represents the extrapolated critical state, based on a least-squares fit of the converged equilibria (dashed blue line). Note that the residual reaction force tolerance at the poker is 0.05 N. (For interpretation of the references to colour in this figure legend, the reader is referred to the web version of this article.)

increasing $u_a$, *i.e.* the size of the dimple decreases as axial compression increases. To prevent the shell from buckling, the path-following procedure is terminated before $u_p = 0$ is reached, and the critical state is extrapolated using a linear least-squares fit (dashed line in Fig. 12b). The extrapolated buckling compression $u_{a,cr} = 0.2400$ mm, is within 2% of the critical value obtained from a linear eigenvalue analysis ($u_{cl} = Lt/(R\sqrt{3(1-\nu^2)}) = 0.2355$ mm). This demonstrates the feasibility of predicting the buckling load of a cylinder by extrapolating the equilibrium curve of the unstable single dimple.

The buckling load of imperfect cylinders is known to fall significantly below linear eigenvalue predictions. Hence, if the above analysis is repeated for an imperfect cylinder, the extrapolated equilibrium curve of the single dimple is expected to predict a buckling load well below the linear eigenvalue prediction. To simulate the effect of geometric imperfections, we seed a random imperfection distribution onto the cylinder. The geometry of the imperfect cylinder is given by:

$$\begin{aligned} x &= [R + A_0 \text{rand}(-1,1)]\cos\theta, \\ y &= [R + A_0 \text{rand}(-1,1)]\sin\theta, \\ z &= z, \end{aligned} \tag{33}$$

where $A_0$ is the imperfection amplitude, $\text{rand}(-1,1)$ is a random number between $-1$ and 1, and $\theta$ and $z$ are the circumferential and axial coordinates, respectively.

Since effective shape control of the structure at unstable equilibria is a prerequisite of the proposed experimental path-following technique, the poker should be located where the localised dimple initially develops. A previous study (Groh and Pirrera, 2019) has shown that localisations generally form at the location with the sharpest imperfection feature, *i.e.* the largest second derivative of the imperfection signature. For modelling convenience, the imperfection amplitude at the poker location is set 10 times greater than at any other location. Numerical path-following using the Riks solver in ABAQUS verifies that the cylinder always buckles by forming a single dimple at this location. Two representative poker locations at axial positions $z_p/L$ = 1/2 and 2/3 are investigated with imperfection amplitude $A_0/t = 0.3$ to consider different imperfection features.

Following the same test procedure, the imperfect cylinder is initially compressed and then poked to obtain the single-dimple solution. Fig. 13a presents the relationship between the poker reaction force and the poker displacement for the imperfect cylinder at different levels of axial compression. Compared to the perfect case, imperfections create limit points before the single-dimple solution is reached, *i.e.* before $F_p = 0$. Therefore, it is not possible to obtain the single-dimple solution using the single poker in these circumstances. The emergence of limit points in the $F_p$ *vs* $u_p$ relationship is caused by the evolution of the localised dimple. Fig. 14 presents the evolution of the single dimple along the unstable portion of the poking curve (beyond limit points in the $F_p$ *vs* $u_p$ plots). The dimple develops at the localised imperfection, see the red dot in subfigure (b-1), but when the axial compression decreases below a certain threshold, the dimple moves away from the original location. Accordingly, the poker will lose control authority over the deformation leading to instability. Therefore, the pre-compression level needs to be sufficiently high for the single dimple to be located at the poking point.

The initial pre-compression level $u_aR/Lt$ in the cylinder is set to 0.3855, *i.e.* $u_a/u_{a,cr}^{perf} = 63.7\%$. The poker reaction force *vs* poker displacement relationship is presented as a solid black line in Fig. 13. Fig. 13b presents the converged single-dimple solution of the imperfect cylinder using the virtual experimental path-following technique. Since the geometric imperfection breaks the subcritical bifurcation on the fundamental prebuckling path, we can path-

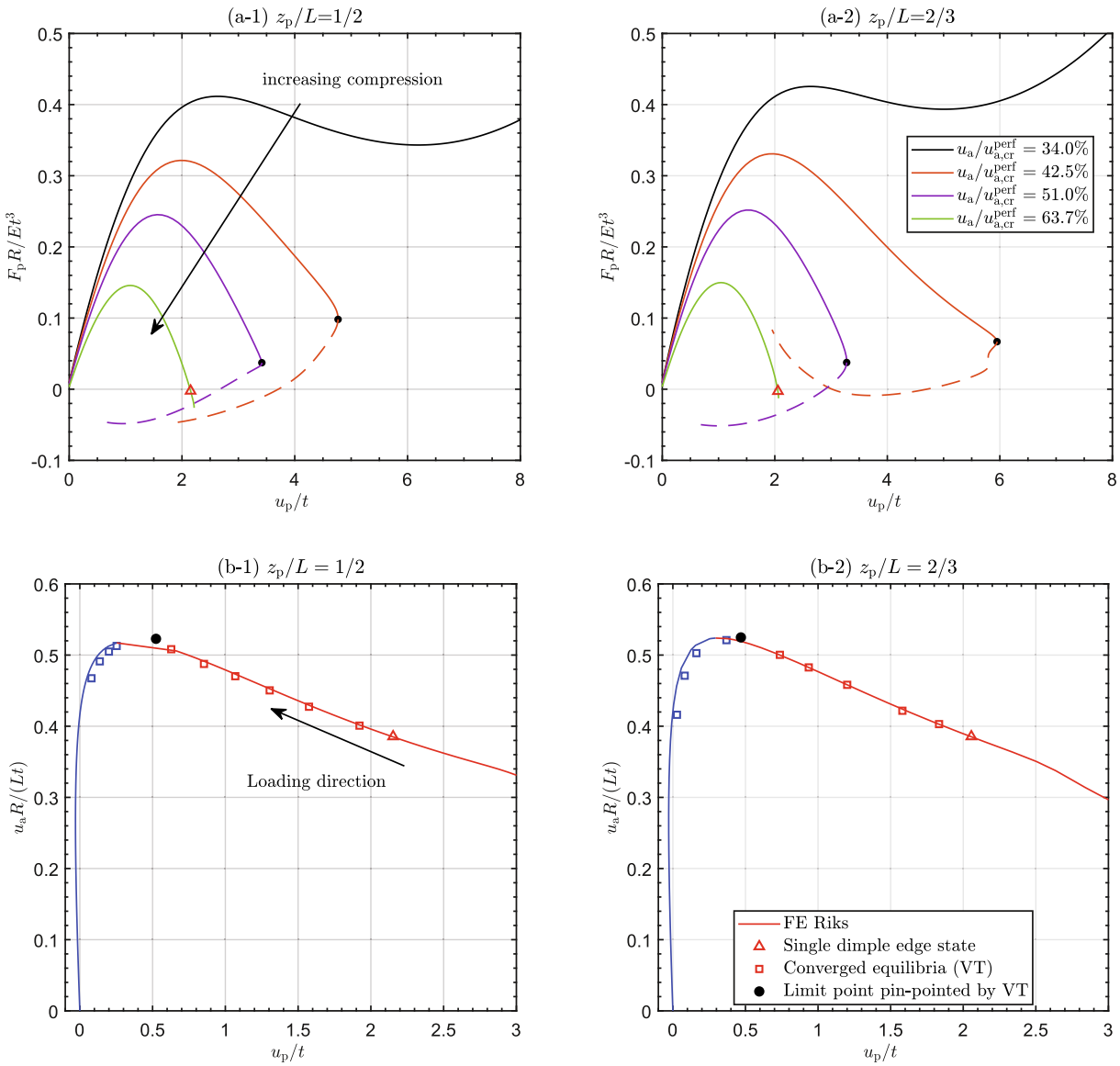


**Fig. 13.** (a) Stability landscape of an axially compressed imperfect cylinder with a poking side force applied at different cylinder axial positions $z_p/L$. Normalised poker force ($F_pR/Et^3$) versus the normalised poker displacement ($u_p/t$) for different levels of axial compression. Solid and dashed lines represent stable and unstable equilibria in terms of displacement-controlled loading. Black dots represent limit points; triangles represent the single dimple solutions, *i.e.* the starting point for the experimental path-following process. (b) Virtual non-destructive testing of imperfect cylinder with localised imperfection. The limit point indicates the predicted buckling load, separating the stable (blue line) and unstable (red line) equilibria. (For interpretation of the references to colour in this figure legend, the reader is referred to the web version of this article.)

follow a continuous equilibrium path and pinpoint the limit point. Note that the relationship between $u_a$ and $u_p$ is almost linear before the limit points for both poking locations. For verification purposes, the static Riks solver within ABAQUS is also used to trace the equilibrium path of the imperfect cylinder under axial compression. Good correlation with the virtual testing results for both poking locations is observed in Fig. 13b. Furthermore, the buckling load predicted by the non-destructive testing methodology is well below the linear eigenvalue prediction, *i.e.* $P/P_{cr} \approx 0.52$. Hence, the buckling load of an imperfect cylinder can be determined experimentally without causing the cylinder to buckle and potentially induce permanent damage.

It should be noted that the proposed non-destructive testing method based within the current experimental path-following framework is only effective if the governing failure mode of the cylinder is a localised single dimple and the poker is located at the strongest imperfection feature. In practice, a surface scanning device would be required to obtain the imperfection profile and determine the best poker location.

As shown in Fig. 13a, the location of the force limit points in the $F_p$ *vs* $u_p$ curves (max $F_p$) are not affected to the same extent by geometric imperfections as the edge state ($F_p = 0$). In other words, the poker does not have to be located at strongest imperfection feature to control the single-dimple deformation shape of the cylinder. Thus, fold line tracing of the ridge (max $F_p$ limit points) is expected to be a more robust non-destructive testing approach. To facilitate this, a force-based experimental path-following framework has to be implemented.

## 4. Conclusions

In Part II we have extended the experimental path-following framework introduced in Part I to the analysis of critical points. Established numerical algorithms for pinpointing critical points, branch-switching at bifurcations and tracing fold lines were described and then implemented in a feedback control system for displacement-based experimental path-following. The feasibil-

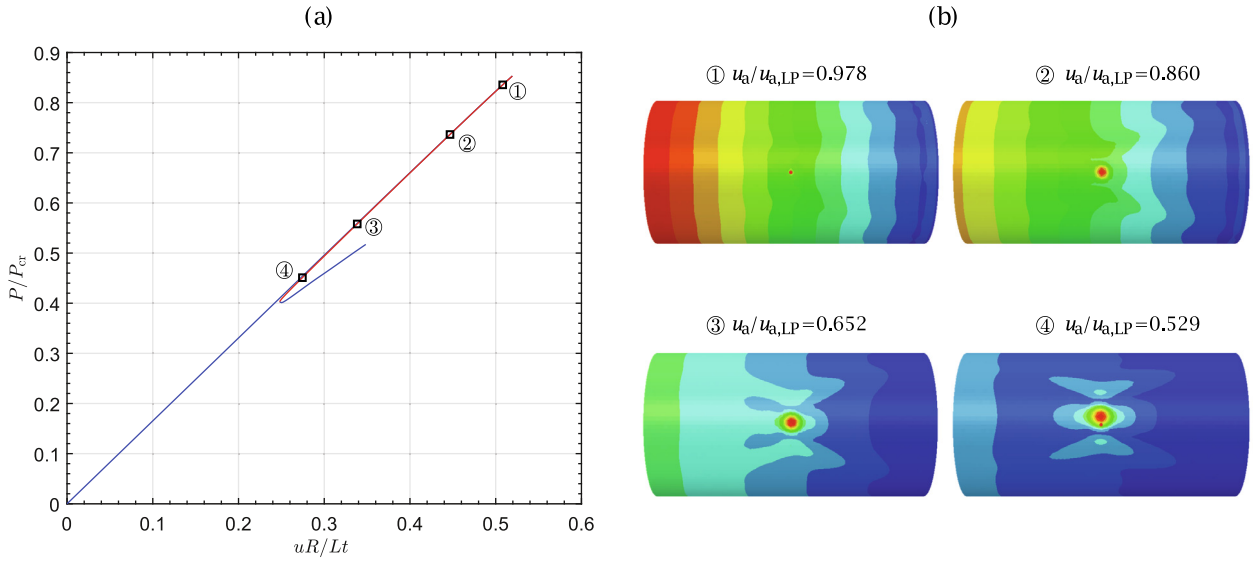


**Fig. 14.** (a) The axial compression load–end-shortening relationship of the imperfect cylinder with four representative deformation shapes of the cylinder on the unstable path presented in (b), solved using the static Riks solver within ABAQUS. Contours show displacement magnitude, with warmer colours indicating larger values. The initial imperfection with magnitude $A_0/t = 0.3$ was located at the half-cylinder length, as indicated by the red dots in (b). Note that the blue and red lines in (a) represent stable and unstable equilibria, respectively. (For interpretation of the references to colour in this figure legend, the reader is referred to the web version of this article.)

ity of these control algorithms was demonstrated via a virtual testing environment, using FE to simulate the nonlinear structures.

Three applications were explored to illustrate the potential of advanced experimental path-following methods: (i) quantifying the sensitivity of snap-through loads in shape-adaptive structures with respect to governing parameters of these structures; (ii) validation of long-standing nonlinear FE benchmark problems; and (iii) a non-destructive testing method for buckling of imperfection-sensitive cylinders governed by a subcritical bifurcation.

The physical implementation of advanced experimental path-following methods will require significant future work. In particular, the integration of multiple independent actuators (and corresponding sensors) for probe and actuation points will complicate the experimental design, and robustness to experimental uncertainty must be further characterised. However, we hope that the examples have demonstrated the potential of the experimental path-following algorithms to facilitate bespoke testing capabilities, and that the results will encourage implementation of these concepts in the fields of experimental mechanics.

## Data Statement

Data are available at the University of Bristol data repository, data.bris, at https://doi.org/10.5523/bris.932lqv3akioz2jrwngdxzshfo.

## Declaration of Competing Interest

The authors declare that they have no known competing financial interests or personal relationships that could have appeared to influence the work reported in this paper.

## Acknowledgments

R.M.J.G. is funded by the Royal Academy of Engineering under the Research Fellowship scheme [Grant No. RF|201718|17178]. J. S. and A.P. are funded by the UK Engineering and Physical Sciences Research Council [Grant No. EP/M013170/1].

## References

Seydel, R., 1979. Numerical computation of branch points in nonlinear equations. Numer. Math. 33 (3), 329–352.
Wagner, W., Wriggers, P., 1988. A simple method for the calculation of postcritical branches. Eng. Comput. 5, 103–109.
Eriksson, A., 1994. Fold lines for sensitivity analyses in structural instability. Comput. Methods Appl. Mech. Eng. 114, 77–101.
Crisfield, M.A., 1981. A fast incremental/iterative solution procedure that handles "snap-through". Comput. Struct. 13, 55–62.
Crisfield, M.A., 1991. Non-linear Finite Element Analysis of Solids and Structures, vol. 2. John Wiley & Sons.
Shen, J., Groh, R.M.J., Schenk, M., Pirrera, A., 2021. Experimental path-following of equilibria using newton's method. Part I: theory, modelling, experiments. Int. J. Solids Struct. 210–211, 203–223.
Shi, J., 1996. Computing critical points and secondary paths in nonlinear structural stability analysis by the finite element method. Comput. Struct. 58 (1), 203–220.
Griewank, A., Reddien, G.W., 1984. Characterization and computation of generalized turning points. SIAM J. Numer. Anal. 21 (1), 176–185.
Kreilos, T., Schneider, T.M., 2017. Fully localized post-buckling states of cylindrical shells under axial compression. Proc. Roy. Soc. A. 473, 20170177.
Renson, L., Sieber, J., Barton, D.A.W., Shaw, A.D., Neild, S.A., 2019. Numerical continuation in nonlinear experiments using local gaussian process regression. Nonlinear Dyn. 98 (4), 2811–2826.
Groh, R.M.J., Pirrera, A., 2019. Spatial chaos as a governing factor for imperfection sensitivity in shell buckling. Phys. Rev. E 100. 032205.
Huitfeldt, J., 1991. Nonlinear eigenvalue problems -prediction of bifurcation points and branch switching. In: Technical report. Chalmers University of Technology and the University of Göteborg.
Riks, E., 1979. An incremental approach to the solution of snapping and buckling problems. J. Solids Struct. 15, 529–551.
Arena, G., Groh, R.M.J., Brinkmeyer, A., Theunissen, R., Weaver, P.M., Pirrera, A., 2017. Adaptive compliant structures for flow regulation. Proc. Roy. Soc. A 473, 20170334.
Arena, G., Groh, R.M.J., Theunissen, R., Weaver, P.M., Pirrera, A., 2018. Design and testing of a passively adaptive inlet. Smart Mater. Struct. 27. 085019.
Groh, R.M.J., Avitabile, D., Pirrera, A., 2018. Generalised path-following for well-behaved nonlinear structures. Comput. Methods Appl. Mech. Eng. 331, 394–426.
Eriksson, Anders, 1991. Derivatives of tangential stiffness matrices for equilibrium path descriptions. Int. J. Numer. Meth. Eng. 32 (5), 1093–1113.
Zhou, Y., Stanciulescu, I., Eason, T., Spottswood, M., 2015. Nonlinear elastic buckling and postbuckling analysis of cylindrical panels. Finite Elem. Anal. Des. 96, 41–50.

Groh, R.M.J., Pirrera, A., 2017. Exploring islands of stability in the design space of cylindrical shell structures. In: Shell Structures: Theory and Applications Volume 4, CRC Press, pp. 223–226..
Wardle, B.L., 2008. Solution to the incorrect benchmark shell-buckling problem. AIAA J. 46 (2), 381–387.
Groh, R.M.J., Pirrera, A., 2018. Orthotropy as a driver for complex stability phenomena in cylindrical shell structures. Compos. Struct. 198, 63–72.
Weingarten, V.I., Morgan, E.J., Seide, P., 1965. Elastic stability of thin-walled cylindrical and conical shells under axial compression. AIAA J. 3, 500–505.
Wagner, H.N.R., Hühne, C., Niemann, S., 2017. Robust knockdown factors for the design of axially loaded cylindrical and conical composite shells – development and validation. Compos. Struct. 173, 281–303.
Evkin, A., Krasovsky, V., Lykhachova, O., Marchenko, V., 2019. Local buckling of axially compressed cylindrical shells with different boundary conditions. Thin-Walled Struct. 141, 374–388.
Groh, R.M.J., Pirrera, A., 2019. On the role of localizations in buckling of axially compressed cylinders. Proc. Roy. Soc. A 475, 20190006.
Virot, E., Kreilos, T., Schneider, T.M., Rubinstein, S.M., 2017. Stability landscape of shell buckling. Phys. Rev. Lett. 119. 224101.